

The VLT-FLAMES survey of massive stars: atmospheric parameters and rotational velocity distributions for B-type stars in the Magellanic Clouds^{*}

I. Hunter^{1,2}, D.J. Lennon^{2,3}, P.L. Dufton¹, C. Trundle¹, S. Simón-Díaz⁴, S.J. Smartt¹, R.S.I. Ryans¹, and C.J. Evans⁵

¹ Astrophysics Research Centre, School of Mathematics & Physics, The Queen's University of Belfast, Belfast, BT7 1NN, Northern Ireland, UK

² The Isaac Newton Group of Telescopes, Apartado de Correos 321, E-38700, Santa Cruz de La Palma, Canary Islands, Spain

³ Instituto de Astrofísica de Canarias, 38200 La Laguna, Tenerife, Spain

⁴ LUTH, Observatoire de Meudon, 5 Place Jules Janssen, 92195, Meudon Cedex, France

⁵ UK Astronomy Technology Centre, Royal Observatory, Blackford Hill, Edinburgh, EH9 3HJ

Received; accepted

ABSTRACT

Aims. We aim to provide atmospheric parameters and rotational velocities of a large sample of O- and early B-type stars, analysed in a homogeneous and consistent manner, for use in constraining theoretical models.

Methods. Atmospheric parameters, stellar masses and rotational velocities have been estimated for approximately 250 early B-type stars in the Large (LMC) and Small (SMC) Magellanic Clouds from high-resolution VLT-FLAMES data using the non-LTE TLUSTY model atmosphere code. This data set has been supplemented with our previous analyses of some 50 O-type stars (Mokiem et al. 2006, 2007) and 100 narrow-lined early B-type stars (Hunter et al. 2006, Trundle et al. 2007) from the same survey, providing a sample of ~ 400 early-type objects.

Results. Comparison of the rotational velocities with evolutionary tracks suggest that the end of core hydrogen burning occurs later than currently predicted. We also show that the large number of the luminous blue supergiants observed in the fields are unlikely to have directly evolved from main-sequence massive O-type stars as neither their low rotational velocities or position on the H-R diagram are predicted. We suggest that blue-loops or mass-transfer binary systems may populate the blue supergiant regime. By comparing the rotational velocity distributions of the Magellanic Cloud stars to a similar Galactic sample we find that (at 3σ confidence level) massive stars (above $8M_{\odot}$) in the SMC rotate faster than those in the solar neighbourhood. However there appears to be no significant difference between the rotational velocity distributions in the Galaxy and the LMC. We find that the $v \sin i$ distributions in the SMC and LMC can modelled with an intrinsic rotational velocity distribution which is a Gaussian peaking at 175 km s^{-1} (SMC) and 100 km s^{-1} (LMC) with a $\frac{1}{e}$ half width of 150 km s^{-1} . We find that in NGC346 in the SMC, the $10\text{-}25 M_{\odot}$ main-sequence stars appear to rotate faster than their higher mass counterparts. It is not expected that O-type stars spin down significantly through angular momentum loss via stellar winds at SMC metallicity, and hence this could be a reflection of mass dependent birth spin rates. Recently Yoon et al. (2006) have determined rates of GRBs by modelling rapidly rotating massive star progenitors. Our measured rotational velocity distribution for the $10\text{-}25M_{\odot}$ stars is peaked at slightly higher velocities than they assume, supporting the idea that GRBs could come from rapid rotators with initial masses as low as $14 M_{\odot}$ at low metallicities.

Key words. stars: early-type – stars: atmospheres – stars: rotation – stars: evolution – Magellanic Clouds

1. Introduction

The evolution of massive stars has traditionally been described in terms of mass and metallicity. However in the past 20 years it has become evident that rotational effects are equally important, from star formation through to their deaths in supernovae explosions and associated gamma-ray bursts (Woosley & Heger 2006). For example, Heger & Langer (2000) discuss how rotation changes the lifetime and evolution of massive stars on the Hertzsprung-Russell

diagram through rotationally induced mixing between the core and envelope.

Rotational effects are also believed to be metallicity dependent. At low metallicity, line-driven winds are weaker and mass-loss rates lower (Kudritzki et al. 1987; Kudritzki & Puls 2000; Vink et al. 2001; Mokiem et al. 2006). Hence a star will lose less angular momentum and thereby maintain higher rotational velocities on the main-sequence. This promotes rotational mixing over a longer period of an object's evolution which in turn extends its lifetime. **Additionally nucleosynthetically processed material will** be mixed from the core into the photosphere and hence abundance anomalies are expected, with helium and nitrogen enhancements and carbon and oxygen depletions. Recent observa-

Send offprint requests to: I. Hunter,
e-mail: I.Hunter@qub.ac.uk

^{*} Based on observations at the European Southern Observatory in programmes 171.0237 and 073.0234

tions of massive stars have revealed abundance anomalies in O-stars (Bouret et al. 2003, Mokiem et al. 2006, 2007), B-type supergiants (Dufton et al. 2005, Hunter et al. 2007, Lennon et al. 2003 and Trundle & Lennon 2005), B-type main-sequence stars (Hunter et al. 2007, Korn et al. 2002, 2005), A-type supergiants (Venn 1999) and lower mass stars (Smiljanic et al. 2006).

Maeder & Meynet (2001) have included rotation and metallicity effects in stellar evolutionary models to explain both the relative frequency of blue and red supergiants as well as observed abundance trends in A-type supergiants at low metallicity. However much remains uncertain. For example, they adopt initial rotational velocities of 300 km s^{-1} , which equates to an average main-sequence rotational velocity of $220\text{-}240 \text{ km s}^{-1}$ (there being little change in the rotational velocity over the main-sequence lifetime of a B-type star), but statistically significant observational samples are necessary both to estimate typical rotational velocities as well as to calibrate the effect of metallicity on the rotational velocities. Additionally rotation has been described as the key ingredient in enabling single stars to explode with associated long-duration gamma-ray bursts by Woosley & Heger (2006), although rotational velocities close to 400 km s^{-1} are required and hence gamma-ray bursts would be relatively rare events compared to supernovae. The requirement that little angular momentum is lost during their stellar lifetime obviously favours low metallicity regimes with their smaller mass-loss rates.

A large survey of massive stars has been undertaken at the European Southern Observatory using the Fibre Large Array Multi-Element Spectrograph (FLAMES) on the 8.2m Keuyen Very Large Telescope. The observations are discussed in detail in Evans et al. (2005, hereafter Paper I) and Evans et al. (2006, hereafter Paper II) and are summarised in Sect. 2. Briefly, some 750 stars have been observed with mainly O and early B spectral types in the Galaxy and the Large (LMC) and Small (SMC) Magellanic Clouds. The analysis of many of these objects is well underway or completed. Mokiem et al. (2006, 2007) have derived atmospheric parameters and helium abundances for the majority of the O-type stars in the sample and discuss the dependence of mass-loss rates on metallicity and calibrate the wind-momentum luminosity relation. Hunter et al. (2007) and Trundle et al. (2007) have derived atmospheric parameters and metal abundances (CNO in particular) for a subset of the narrow-lined B-type main-sequence and supergiant stars finding that significant mixing has occurred in many of the objects. Dufton et al. (2006, hereafter Paper III) have estimated atmospheric parameters and rotational velocities of the entire Galactic sample and report that more massive stars have lower rotational velocities (as expected from enhanced mass-loss) and that cluster objects appear to rotate significantly faster than objects in the Galactic field.

In order to examine the effects of rotation, here we perform a similar analysis to Paper III and estimate atmospheric parameters and rotational velocities for the Magellanic Cloud sample of B-type stars. **The principle intention of performing such an analysis was to provide rotational velocities for a large sample of early-type stars in a homogenous and consistent manner. This dataset can then be used to answer several questions of importance to massive star evolution:**

- **Where does the end of core hydrogen burning occur and how can large populations of post core hydrogen burning objects be explained?**
- **Are the rotational velocities of early B-type stars dependent on the metallicity of the host environment?**
- **Are mass-loss effects important at low metallicity and how do these affect the predictions of gamma-ray burst rates from massive star progenitors?**

In Sect. 2 we briefly describe the FLAMES survey and our selection criteria for the objects discussed here. In Sect. 3 we present our methods for deriving the atmospheric parameters and projected rotational velocities. **In Sect. 4 the rotational velocity distributions of the different subsets of the sample (for example, binaries, Be-type stars, high mass stars and supergiants) are compared. In Sect. 5 the relevant subsets are utilised to answer the three questions posed above.** Finally in Sect. 6 we present the principal conclusions from our analysis.

2. Observations

As part of a European Southern Observatory (ESO) Large Programme on the Very Large Telescope (VLT, Paranal, Chile) observations were obtained for over 700 stars using the Fibre Large Array Multi-Element Spectrograph (FLAMES), with the majority of these objects being O- or early B-type stars. Observations were taken towards three Galactic clusters, NGC 6611, NGC 3293 and NGC 4755; two LMC clusters, N 11 and NGC 2004 and two SMC clusters, NGC 346 and NGC 330. Details of the observational fields, target selection and data reduction were discussed in Paper I and Paper II¹. The FLAMES spectroscopy covered the wavelength regions $3850\text{-}4755 \text{ \AA}$ and $6380\text{-}6620 \text{ \AA}$ and was supplemented with additional observations from the Fiber-fed Extended Range Optical Spectrograph (FEROS) and the Ultraviolet and Visual Echelle Spectrograph (UVES), both of which had a more extensive wavelength coverage. To maintain consistency throughout the analysis we only consider the FEROS and UVES data in the same wavelength range as that of the FLAMES observations.

2.1. Radial velocity corrections and binarity

Observations were taken in six wavelength settings in order to achieve our desired wavelength coverage at high spectral resolution, with multiple exposures (typically six) being taken in each setting. **However, in cases where exposures are of significantly lower quality than the norm, these have been excluded.**

To increase the signal to noise (S/N) ratio of the data, it is possible to combine the individual exposures in each set-

¹ We note that in Paper II the radial distance of the NGC 346 objects from the centre of the association was calculated based on the NGC 346 centre obtained from the SIMBAD database (operated at the CDS, Strasbourg, France) which is actually the centre of the ionised shell of gas and is offset from the centre of the OB association. In Table 1 (only available online at the CDS) the radial distances are listed with the centre taken as the position of object 435 from the Massey et al. (1989) catalogue of OB stars in NGC 346; $\alpha(2000) = 00 \text{ } 59 \text{ } 04.49$ $\delta(2000) = -72 \text{ } 10 \text{ } 24.7$.

ting. However, it is first necessary to check for radial velocity shifts between exposures, an indicator of binarity. IDL procedures have been developed to cross-correlate each exposure in the FLAMES data and identify significant radial velocity shifts at the 3σ level (see Hunter et al. 2007). We note that this procedure is superior to that used in Papers I and II where binaries were identified by eye from the combined spectra of the exposures in each wavelength setting. Our cross-correlation procedure has identified additional binaries not previously detected in Paper II. Additionally for several stars we find that the radial velocity shifts detected in Paper II are not significant at the 3σ level and hence we do not consider them as binary stars. We note that most of these objects were identified as possible binaries in Paper II or had Be classifications and large rotational velocities, which makes binary detection uncertain. After correction for velocity shifts, IRAF routines were used to combine the exposures and simultaneously remove cosmic rays. This procedure was not possible for the double lined spectroscopic binaries and the analysis of these systems (where this was possible) is discussed in Sect. 3.5. Throughout this paper all radial velocity variables are considered as binary objects although our temporal resolution is not sufficient to derive periods and other orbital parameters to confirm if they truly are all binary stars.

2.2. Selection criteria

We have selected objects with spectral types later than O9 and earlier than B9 which can be analysed with our non-LTE TLUSTY model atmosphere grid which has an effective temperature range from 12 000 K to 35 000 K (see Sect. 3.1). The majority of the O-type stellar sample observed in the FLAMES survey has been analysed by Mokiem et al. (2006, 2007) for the SMC and LMC O-type stars respectively.

We have attempted to derive parameters for every object in our spectral type range but this was not possible for a small minority. Typically objects were excluded if it was not possible to separate individual spectra in a double lined binary system, if the spectra were not of sufficient quality to reliably estimate velocity corrections in the case of single lined spectroscopic binaries or if the stellar spectra appeared to be variable between exposures. Additionally a few objects have been excluded as shell absorption contaminated both the hydrogen and helium lines and no metal lines were well enough observed to allow for a reliable determination of the rotational velocity. In Table 2 we list those objects within our spectral type range that have been excluded. These objects form less than 6% of the sample, with the majority being binaries and having either Be classifications or uncertain spectral types.

2.3. Field populations

In Paper II images of the four regions are displayed and it is clear that the majority of our objects do not lie within the core of the clusters, due to constraints in positioning the fibres of the FLAMES instrument. Specifically for the NGC 330 and NGC 2004 fields, our samples are probably dominated by field objects. NGC 346 does not have a compact core and it is difficult to determine the extent of the cluster. Indeed, NGC 346 is often described as an OB as-

Table 2. Objects with spectral types later than O9 and earlier than B9 observed in the FLAMES survey that have been excluded from this analysis.

Cluster	Excluded stars
NGC 346	017, 038, 060, 086, 105, 111, 115
NGC 330	030, 077, 088, 092, 093, 115, 117
N 11	005, 030, 053, 067, 099, 112
NGC 2004	019, 028, 033, 034, 037, 038, 072

sociation rather than as a bound cluster (see for example Gouliermis et al. 2006). N 11 is dominated by two distinct regions, LH 9 and LH 10, where sequential star formation has occurred. Additionally there are many smaller pockets of star formation within this region complicating the picture further.

The supergiant objects in NGC 330 are not located close to or in the core of NGC 330; they instead appear to be randomly distributed in the field and may indicate that they are indeed field stars. However, it should be noted that almost no supergiants are observed towards NGC 346, implying an age difference between NGC 346 and NGC 330. Similarly to NGC 330 the supergiants observed towards N 11 and NGC 2004 are not clustered in one region. Additionally in N 11 the O-type stars are not clustered in the younger LH 10 region, indicating that the OB association is probably not bound.

As such our four Magellanic Cloud samples are probably better described as unbound associations with the association ‘evaporating’ as their OB stars become part of the field population. Sirianni et al. (2002) have obtained colours for the stars in both the central and outer regions of NGC 330 and find remarkable similarity between the regions implying that NGC 330 may extend well beyond its dense core. The recent review of Bastian & Gieles (2006) describes the various phases of cluster disruption, in particular that of ‘infant mortality’, where through gas expulsion during cluster formation the cluster becomes unbound, and if the star formation efficiency is low, the cluster can become unbound on the order of a few tens of Myr (see the recent work of Goodwin & Bastian 2006 and references therein).

3. Analysis

3.1. Non-LTE TLUSTY model atmosphere grids

The non-LTE TLUSTY model atmosphere grids (see Hubeny & Lanz 1995 and references therein) used in this analysis have previously been discussed – see Hunter et al. (2007) for an overview of the grids and Dufton et al. (2005) for a detailed discussion².

Briefly, model atmosphere grids have been calculated for the analysis of B-type stellar spectra, covering the effective temperature range from 12 000 K to 35 000 K in steps of not more than 1 500 K, a surface gravity range from the Eddington limit up to 4.5 dex, in steps of 0.15 dex and microturbulence values of 0, 5, 10, 20 and 30 kms^{-1} . Four model atmosphere grids have been generated with metallicities representative of the Galaxy ($[\text{Fe}/\text{H}]=7.5$ dex),

² See also <http://star.pst.qub.ac.uk>

the LMC (7.2 dex), the SMC (6.8 dex) and a lower metallicity regime (6.4 dex). A nominal helium abundance of 11.0 dex has been adopted throughout. Theoretical spectra and metal line equivalent widths have then been calculated for each grid point.

3.2. Atmospheric parameters

Hydrogen and helium lines are observable in the spectra of all our targets and these lines have been used as the primary indicators of effective temperature and surface gravity. IDL procedures have been developed which fit model spectra (convolved with an appropriate stellar broadening function) of the appropriate metallicity to the observed hydrogen and helium lines and calculate the region of best fit (by chi-squared minimisation) in effective temperature - surface gravity space. As these parameters are interdependent it is necessary to use an iterative method. In Paper III equivalent width measurements of the hydrogen and helium lines were used to constrain the atmospheric parameters but we believe that the ‘profile fitting’ methodology we have adopted here is an improvement as it uses both information on the line strength and shape. We estimate that this methodology results in a typical uncertainty of 1 500 K for the effective temperature, with that for the surface gravity being discussed below.

The He I spectrum is a suitable effective temperature indicator at spectral types of approximately B3 and later, while the He II spectrum can be used to constrain the temperature of stars with a spectral type of B1 or earlier. Hence there remains a range of spectral types where the He II lines are not observed and the He I spectra are not sensitive to temperature. For spectra with narrow metal absorption lines, where two ionization stages of silicon were observed, it is possible to use the silicon ionization balance to constrain the effective temperature, with the surface gravity again being estimated from the hydrogen lines. Hunter et al. (2007) and Trundle et al. (2007) have presented analyses of the narrow lined B-type stars in the FLAMES survey and their atmospheric parameters have been adopted. For stars with large projected rotational velocities in the B1-3 spectral type range, it was not possible to observe two stages of silicon ionization. As in Paper III, we have adopted effective temperature-spectral type calibrations. These are based on the analysis of the narrow lined objects and are presented in Trundle et al. for both LMC and SMC metallicities.

Both the H δ and H γ absorption lines have been observed in our spectra and these have been used to estimate the surface gravity by the method of profile fitting described above. In the majority of cases we find excellent agreement between the estimate derived from each line with differences typically being less than 0.15 dex. The effective temperature and surface gravity estimates are directly correlated and an over estimate of the effective temperature by 1 000 K will lead to an over estimate of the surface gravity by approximately 0.1 dex. Hence we believe that our surface gravity estimates should be typically accurate to 0.2-0.25 dex.

It has previously been found that there is a correlation between surface gravity and microturbulence with supergiants typically having greater values of microturbulence than giant and main-sequence stars (see for example Gies & Lambert 1992). Representative microturbulence values of 10 and 5 km s⁻¹ have been adopted for supergiants and the less evolved objects respectively. It should be noted that

this choice has a negligible effect on the atmospheric parameters and only affects the projected rotational velocity estimate when the measured values are less than 20 km s⁻¹. The atmospheric parameters are listed in Tables 3-6, only available online at the CDS. In these tables we give the star identifier and spectral type (from Paper II), the effective temperature, surface gravity, projected rotational velocity, adopted methodology, luminosity, mass and additionally indicate if the star is a radial velocity variable and hence probably in a binary system.

3.3. Projected rotational velocities

Several methods are available to estimate projected rotational velocities ($v \sin i$). The most commonly used in the case of OB-type stars are based on a direct measure of the FWHM of the spectral lines (viz. Slettebak et al. 1975; Abt et al. 2002; Herrero et al. 1992; Strom et al. 2005) or profile fitting (Gray 1976; Paper III), while Penny (1996) and Howarth et al. (1997) applied a cross correlation method to IUE spectra. Recently, Simón-Díaz & Herrero (2007) have discussed the utility of the Fourier method (Gray 1976) in the case of early type stars. Each of these methods have their advantages and disadvantages, with for example, the Fourier method being able to deconvolve the rotational broadening from other broadening mechanisms such as macroturbulence, although it requires high quality spectra. Profile fitting to obtain the rotational velocity is possible for lower quality spectra, but relies on an appropriate description of the intrinsic line profile (from a stellar atmosphere code), and the broadening agents affecting the line profile. Measuring the FWHM and using the cross correlating method is relatively straight forward but does not take into account the possible extra non-rotational broadenings (such as Stark broadening of the H and He lines, macroturbulence and microturbulence) thereby leading in some cases to only upper limits for the projected rotational velocity estimate.

Given the quality of our spectra we decided to use the profile fitting methodology discussed in Paper III for all the non-supergiant objects as the quality of our data is not high enough to make the Fourier method viable for the entire sample. Briefly, a model spectrum, at the closest TLUSTY grid point to the derived atmospheric parameters, was selected and the equivalent width of an appropriate line was then scaled to the same strength as that observed. Typically this scaling was less than 10% and, except for the narrowest lined spectra, has little effect on the derived projected rotational velocity. The model profile was first convolved with a Gaussian profile to take into account the spectral resolution of our data; then, the resultant profile was convolved with a rotational broadening function for a range of rotational velocities. A chi-squared minimisation test was used to estimate the projected rotational velocity. The atmospheric parameters were then redetermined with this new estimate and the process repeated. Generally no more than two iterations were required.

Hydrogen lines were observed in all our spectra, but their profiles are dominated by Stark broadening. Although this also affects the diffuse He I lines, at moderate projected rotational velocities, the rotational broadening begins to dominate, and hence they are suitable for estimating this quantity. The He I 4026Å line is observed across all our spectral types and additionally is well separated from other

absorption features. Therefore this line was employed for the profile fitting methodology. Note however, that at low projected rotational velocities the profile of this He I line is no longer sensitive to the rotational broadening. For these cases, we have instead used metal lines if available (typically either the Mg II 4481Å line or the Si III 4552Å line). These projected rotational velocity estimates are listed in Tables 3-6, apart from those of the supergiant targets discussed below.

A small fraction of the objects in our sample have uncertain spectral types that lie in the range B1-3 and, as discussed above, the He line spectrum is not capable of constraining their temperatures. In order to derive the projected rotational velocity of these objects, approximate models have been adopted. As these stars frequently have large rotational velocities (leading to the uncertain spectral classification), the broadening of the observed lines will be rotationally dominated and hence assuming an inappropriate model will not significantly affect the derived rotational velocity. Atmospheric parameters are not given in Tables 3-6 for these objects.

We have also estimated rotational velocities using the Fourier transform methodology where possible. A detailed discussion of the applicability of this methodology in the case of early type stars is given by Simón-Díaz & Herrero (2007) and will not be repeated here. In Fig. 1 we compare the projected rotational velocity derived by the profile fitting methodology and the Fourier transform methodology for the non-supergiant targets, where the spectra were of sufficient quality for the application of the Fourier method. We find in almost all cases good agreement (within 10%), indicating that the choice of methodology is unimportant for these targets and validating our adopted projected rotational velocity estimates.

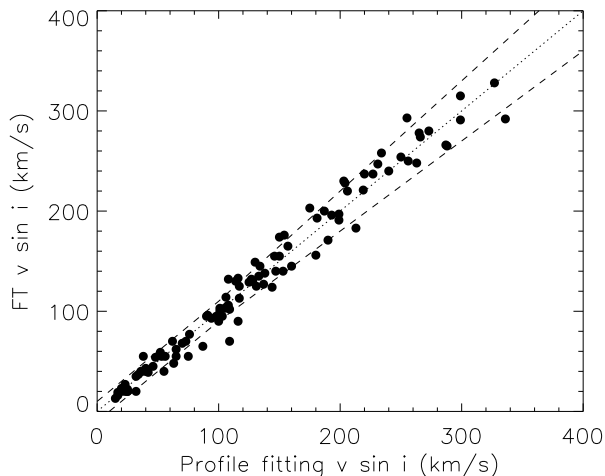


Fig. 1. Comparison of the projected rotational velocity derived by the profile fitting method and the Fourier transform method for the non-supergiant objects in the sample. The dotted line indicates a one-to-one correlation. The dashed lines indicate a 10% or 10 km s^{-1} uncertainty, whichever is the larger.

As already proposed by several authors (Slettebak 1956; Conti & Ebbets 1977; Howarth et al. 1997), and recently

illustrated by Ryans et al. (2002), Dufton et al. (2006b) and Simón-Díaz & Herrero (2007), there is an important non-rotational broadening mechanism affecting the profiles of early type supergiants (usually termed macroturbulence). Since the line fitting methodology does not allow for this extra source of broadening, the Fourier transform technique has been used to derive the projected rotational velocity of objects classed as supergiants in the sample. In Fig. 2 we compare the derived rotational velocities from the two methods for these objects. Due to the quality of the spectra, in terms of signal to noise ratio, in many cases it was only possible to derive upper limits to the projected rotational velocity from the Fourier method (see Simón-Díaz & Herrero); these are indicated by downward pointing arrows in Fig. 2.

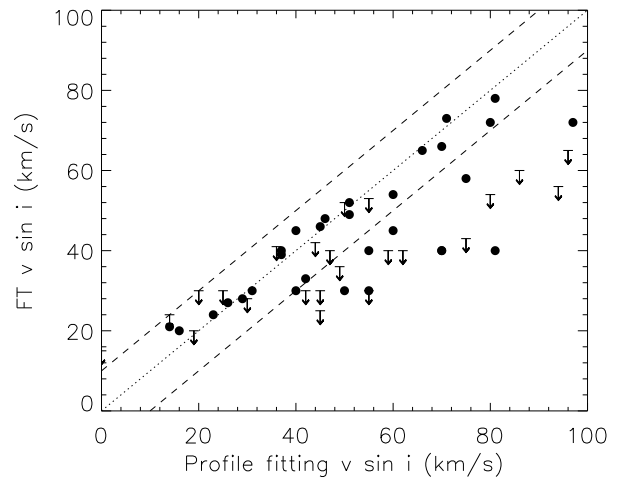


Fig. 2. Comparison of the projected rotational velocity ($v \sin i$) derived by the profile fitting method and the Fourier transform method for the supergiant objects in the sample. The dotted line indicates a one-to-one correlation. The dashed lines indicate a 10 km s^{-1} uncertainty. Downward pointing arrows indicate those objects where it was only possible to derive upper limits to the $v \sin i$ from the Fourier method.

From Fig. 2 it is apparent that in many cases the projected rotational velocities derived from the Fourier Transform method are significantly lower than those from the profile fitting method and these are likely to be objects with significant macroturbulent broadening. Hence for the supergiant targets, the projected rotational velocities listed in Tables 3-6 are those deduced from the Fourier Transform methodology. We note that for the determination of the atmospheric parameters of the supergiant objects in the sample, the estimated rotational velocity determined from the profile fitting method was used rather than that from the Fourier Transform method. This is valid as it is the entire broadening of the line which is important when determining the parameters and not simply the rotational component.

The uncertainties in effective temperature and surface gravity have little effect upon our estimated projected rotational velocities. For example, NGC 346-083 was analysed with a model profile at a temperature of 27500 K and a surface gravity of 4.00 dex and a projected rotational ve-

locity of 207 km s^{-1} was estimated. Adopting a higher temperature profile of $30\,000 \text{ K}$ and higher surface gravity of 4.25 dex (as the surface gravity and effective temperature estimates are directly correlated) leads to a $v \sin i$ estimate of only 4 km s^{-1} greater. Similarly adopting a lower temperature and gravity ($25\,000 \text{ K}$, 3.75 dex) results in a value 14 km s^{-1} greater. Including the effects of normalisation, scaling and choice of model profile we would not expect the errors in our rotational velocity estimates to exceed 10%. This is confirmed by **the comparison shown in Fig. 1** where different lines were used for the Fourier Transform and the profile fitting methods. We note that the Fourier Transform method is additionally model independent.

Rapidly rotating objects (close to critical velocity) can not be considered spherical and equatorial gravity darkening (the cooler and fainter equatorial regions of an oblate star contribute less flux to the observed spectrum) can significantly alter the estimated atmospheric parameters and projected rotational velocities (von Zeipel 1924). Townsend et al. (2004) have shown that this effect leads to an underestimation of projected rotational velocities for close to critical rotational velocities and that the maximum ratio of projected rotational velocity to critical velocity ($v \sin i / v_c$) that can be inferred from line widths is approximately 0.8. We have derived critical rotational velocities for our sample and find that **less than 5% of our sample** have $v \sin i / v_c$ ratios greater than 0.5 with the maximum value of this ratio being approximately 0.7 (NGC 2004-113). If we consider that this object is rotating at near to critical velocity, the projected rotational velocity would be underestimated by less than 15% due to the effects of gravity darkening (Fig. 1, Townsend et al.). Hence we believe that gravity darkening effects should be small compared to our observational uncertainties for the majority of our sample of stars and in the most extreme cases of the same order.

3.3.1. Comparison with other work

Martayan et al. (2006, 2007) have observed a large number of Be and B-type stars towards NGC 2004 and NGC 330 also with the FLAMES instrument, but with lower spectral resolution than we employed. In order to make comparison with the results of Martayan et al. the samples were constrained to the magnitude range where there is a good overlap between them. For NGC 330 this is the visual magnitude range of 15.0-16.5 **with a comparison of the two samples being shown in Fig. 3**. The cumulative probability distributions of the B-type stars closely agree. There is some suggestion that the FLAMES sample contains a larger fraction of stars with very low projected rotational velocities than does the that of Martayan et al. Given the higher spectral resolution and signal to noise ratio of our FLAMES data, this is not unexpected. There are 13 objects in common between our FLAMES survey of NGC 330 and that of Martayan et al. and in Fig. 4 we compare the projected rotational velocities for these stars. In general there is reasonable agreement between the two samples, although the discrepancy at low projected rotational velocities is again evident.

The distributions of the Be stars shown in Fig. 3 are in clear contrast, with Martayan et al. (2007) finding systematically higher projected rotational velocities. The reason for such a large discrepancy is unclear. For the estimation of parameters of their Be sample, Martayan et al. removed the

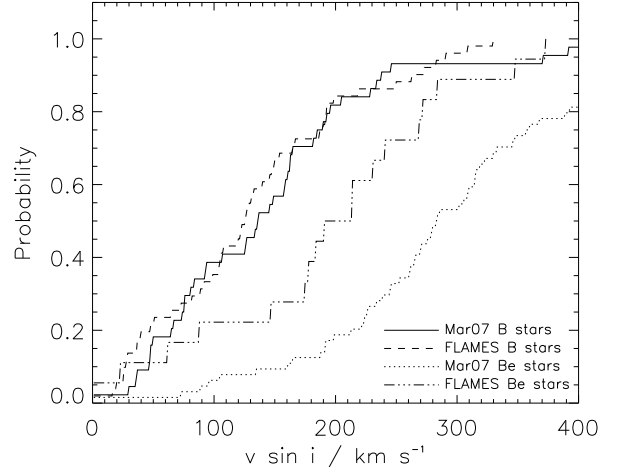


Fig. 3. Comparison of our estimated rotational velocities (FLAMES) with those of Martayan et al. (2007, Mar07) for the B and Be type stars towards NGC 330. **This clearly shows the discrepancy between the Be analysis presented here and that of Martayan et al.** Only objects in the visual magnitude range 15-16.5 have been included.

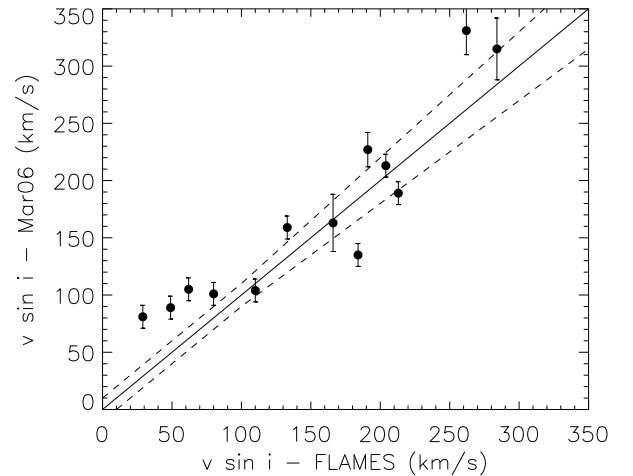


Fig. 4. Comparison of our estimated rotational velocities (FLAMES) with those of Martayan et al. (2007, Mar06). The solid line indicates a one-to-one correlation. The dashed lines indicate our 10% uncertainty down to a limit of 10 km s^{-1} .

core of the lines where Be emission was observed and hence the projected rotational velocities are estimated from the wings of the line. In Fig. 5 we present a comparison between a model spectrum of a $\text{H}\gamma$ line with no rotational broadening and that with a rotational broadening of 300 km s^{-1} . It is clear that the wings are not as sensitive as the line core to changes in the rotational broadening. As such removing the line core will increase the uncertainty of the rotational velocity estimate, especially for low signal to noise data. However, by normally using only one line to determine the projected rotational velocity, our estimates may be biased towards smaller rotational velocities due to saturation ef-

fects (Fremat et al. 2005) compared to those of Martayan et al. who have used several lines, although, this should only be an issue at high rotational velocity. As discussed **above** gravity darkening should be negligible for the objects in our sample. Indeed, for **ten** Be-type objects we have also derived rotational velocities from the He I line at 4387Å and generally find good agreement with the values from the 4026Å line. Additionally in estimating the projected rotational velocities, models with a surface gravity of 4.0 dex have been adopted. At this high gravity the Stark broadening will be relatively large and hence less rotational broadening is required to fit the profile compared to assuming a lower gravity, see Table 7. As such our Be star rotational velocities may be biased towards lower values, but this is only an issue at low projected rotational velocities and in these cases we have endeavored to use metal lines where possible in order to minimize this bias.

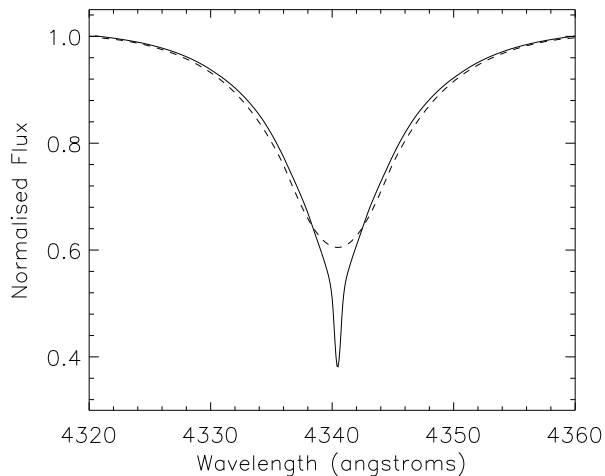


Fig. 5. Comparison of a theoretical H γ line with no rotational broadening (solid line) with the same line rotationally broadened by 300 km s⁻¹ (dashed line) **showing that the wings of the hydrogen line are not sensitive to rotational broadening.**

We have no NGC 2004 objects in common with the sample of Martayan et al. (2006) and the magnitude range of overlap is much smaller than that of the NGC 330 samples although similar trends are seen in the rotational velocity distributions. The B-type stars are in excellent agreement and again there is some evidence that the Be stars of Martayan et al. have higher rotational velocities. Although the discrepancy between the Be star analyses cannot be fully resolved, this does not invalidate the metallicity dependence discussed in **Sect. 5.2. Indeed, since** the SMC has a higher fraction of Be stars than the LMC, using the results of Martayan et al. would enhance the difference between the rotational velocity distributions of the two Magellanic Clouds.

3.3.2. Selection effects

As discussed in Paper II approximately 30 (potential) Be stars were removed from the list of possible targets for the FLAMES pointing towards NGC 330. Given that Be

stars are typically the fastest rotators in the sample, this could bias our velocity distribution towards lower rotational velocities. To investigate this we ran the target selection software, CONFIGURE, again for the NGC 330 field, without explicitly excluding any objects from the input catalogue. From this test we found seven of the previously excluded stars were included in the resulting fibre configuration (which of course differs from our actual observed field by more than seven stars, due to the different positions of the allocated fibres). If we consider that the net difference was to replace seven normal B-type stars with seven Be targets, the mean rotational velocity of the SMC stars would only increase by ~ 3 km s⁻¹. Given that some of the excluded objects are not actually confirmed Be stars this is a conservative estimate, and we believe that any minor selection effect that may have been introduced does not unduly bias our conclusions.

3.4. O-type stars

Atmospheric parameters and projected rotational velocities of the majority of the O-type objects observed Paper II have been derived by Mokiem et al. (2006, 2007) and these have been directly inserted into Tables 3-6. We note that for those stars where our analysis overlaps with that of Mokiem et al. we find good agreement between the two sets of atmospheric parameters and rotational velocities.

3.5. Binary objects

After correcting for radial velocity shifts (see Sect. 2.1), the single lined spectroscopic binaries were analysed using the methodology outlined above. However, this was not possible for the double lined spectroscopic binaries, due to both continuum contamination and the double line nature of the profiles. In Tables 3-6 we indicate those objects for which we see evidence of a secondary object, although for small asymmetries and velocity shifts in the line profile, variability may also be an explanation. For all cases, the individual exposures were examined to find those in which the line profiles from the primary and secondary objects had the maximum separation. The profile fitting methodology was then used to estimate the rotational velocity of the primary, and where possible, the secondary object. We do not attempt to derive atmospheric parameters for either object. Metal lines were used to estimate the rotational velocities in order to minimise the uncertainty from the choice of model profile. An example of the fit for the double lined spectroscopic binary system NGC 346-020 is shown in Fig. 6, where the Si III lines from each object are partially blended. Where it has been possible to estimate the projected rotational velocity of the secondary object in a binary system this is listed in Tables 3-6 with the letter ‘B’ appended to the system’s identifier.

3.6. Be objects

A significant fraction of the stellar sample is made up of Be type objects, with the majority having spectral types in the range B 1-2. In Tables 3-6, we do not give atmospheric parameters for these objects due to problems associated with continuum contamination from the circumstellar disc and emission lines. Additionally as many of the objects do

Table 7. Dependence of the derived $v \sin i$ value upon surface gravity for a sample of Be objects. For large rotational velocities, the Si III lines could not be identified.

Line	log g (dex)	$v \sin i$ (km s ⁻¹)		
		NGC 346-091	NGC 346-095	NGC 346-096
He I 4026Å	4.00	74	227	346
He I 4026Å	3.50	120	250	343
Si III 4552Å	4.00	49	-	-
Si III 4552Å	3.50	47	-	-

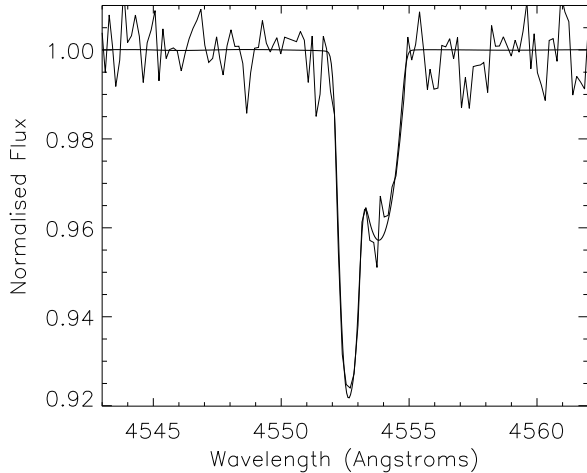


Fig. 6. Fit of the Si III line at 4552Å for the double lined spectroscopic binary system NGC 346-020. The model spectra for the primary and secondary objects have been fitted with a $v \sin i$ value of 34 km s⁻¹ and 66 km s⁻¹ respectively.

not have precise spectral types it was not possible to assign an effective temperature based on spectral type. We have however used the metal line and helium spectra to estimate the projected rotational broadening.

In Table 7 we show how the estimated **projected rotational velocity** depends on the adopted surface gravity for three Be type stars with low, medium and high velocities. It is evident that at large rotational velocities the He profile is dominated by the rotational broadening and is no longer sensitive to the adopted profile. Additionally the projected rotational velocity estimated from the metal line spectra does not appear to be dependent on the adopted model profile and we have adopted these estimates in Tables 3-6 where possible.

3.7. Luminosities

Luminosities were calculated for each object in the sample using the same methodology as discussed in Hunter et al. (2007). Constant values of reddening towards each cluster were assumed, with $E(B - V)$ values of 0.09 (Massey et al. 1995), 0.06 (Gonzalez & Wallerstein 1999), 0.13 (Massey et al.) and 0.09 (Sagar & Richtler 1991) being adopted for NGC 346, NGC 330, N 11 and NGC 2004 respectively. We adopt the SMC reddening law of $A_V = 2.72E(B - V)$ from Bouchet et al. (1985) for the SMC targets while we use the standard Galactic law for the LMC targets. We note that

assuming the standard Galactic law would change the derived SMC luminosities by less than 0.04 dex. Bolometric corrections have been adopted from Vacca et al. (1996) **for objects hotter than 28,000 K** and Balona (1994) **for cooler objects, together with distance moduli** of 18.91 dex (Hilditch et al. 2005) and 18.56 dex (Gieren et al. 2005) for the SMC and LMC. The luminosities are given in Tables 3-6 and typically have an uncertainty of 0.1 dex.

3.8. Masses

In Fig. 7, Hertzsprung-Russell diagrams are presented for the sample of stars towards each cluster. Non-rotating evolutionary tracks are also shown and from these the evolutionary masses of each object have been estimated and these are listed in Tables 3-6. Isochrones are not included as our sample is likely to be dominated by field stars and therefore the populations are unlikely to be coeval, see Sect. 2.3.

The dashed line in Fig. 7 indicates the magnitude limit for our observations in each region (see Paper II) and it is clear that we sample the zero-age main-sequence (ZAMS) at differing masses in each clusters. For example we tend to sample more evolved objects in NGC 2004 due to our target selection, but do sample stars on the ZAMS below 9, 12 and 15 M_{\odot} in NGC 330, NGC 346 and N 11 respectively.

The uncertainty in the masses for those objects for which we have estimated effective temperatures is typically 10-15%, which arises **principally** from the uncertainty in the luminosity. In Tables 3-6 we do not give atmospheric parameters for Be stars, double lined spectroscopic binaries and stars with uncertain spectral types. However, for the estimation of their masses, we assume temperatures based on their spectral type (or their mean spectral type where a spectral type range is given). The uncertainty in the mass of these objects is typically 30%. In addition to these evolutionary masses it is possible to estimate spectroscopic masses, but an uncertainty of 0.25 dex in the surface gravity estimate corresponds to an uncertainty of over 70% in the spectroscopic mass and hence such estimates are of limited value.

3.8.1. Mass discrepancy

Although individual spectroscopic masses are highly uncertain, our sample is large enough to examine systematic differences between evolutionary and spectroscopic masses. For example, it is well known that the evolutionary masses derived for OB-type supergiants typically are greater than the spectroscopic masses (see for example, Herrero et al., 1992; Trundle & Lennon, 2005; Lennon et al., 2003). In Table 8 the average mass discrepancies are summarized. While the discrepancy for evolved stars has previously been

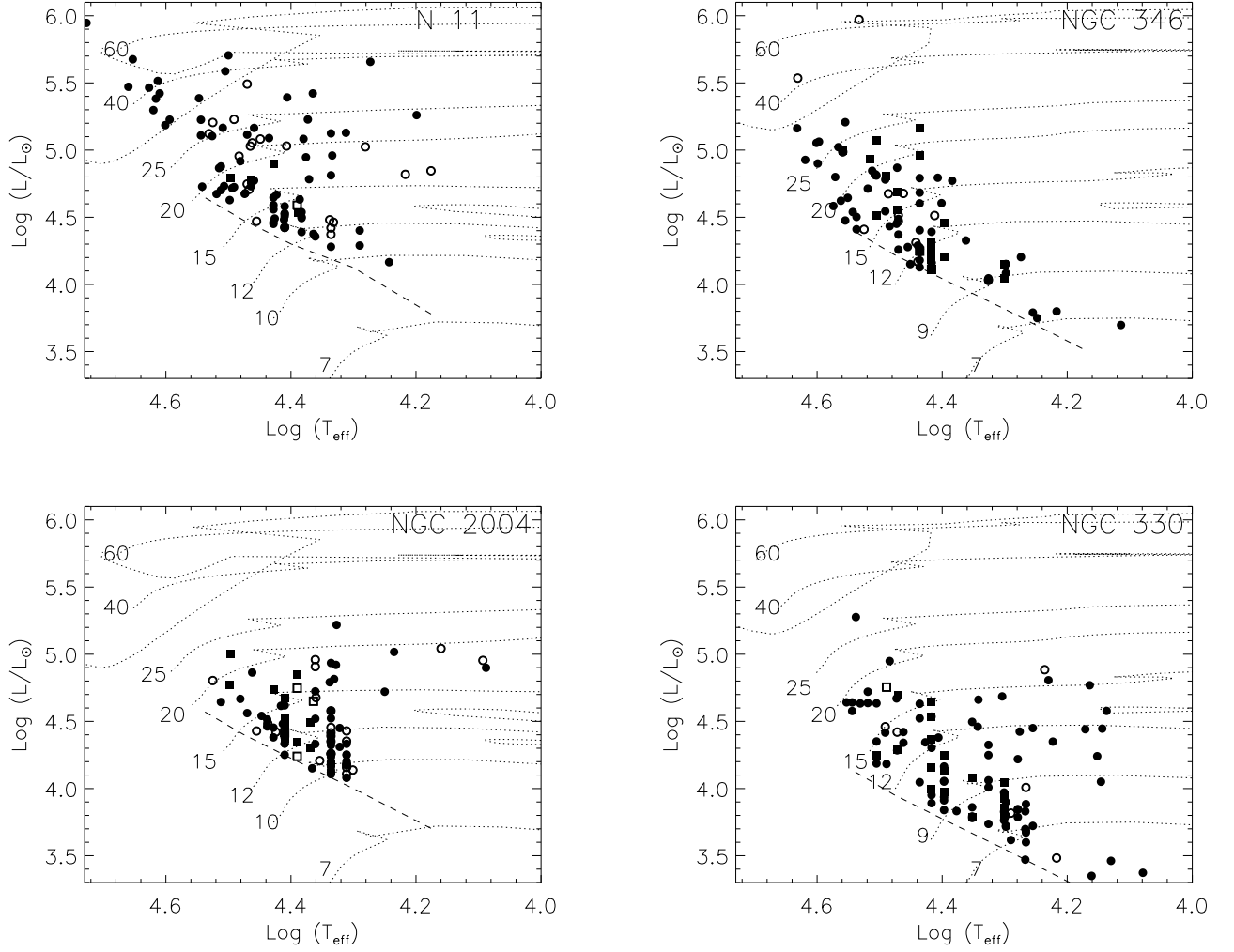


Fig. 7. Hertzsprung-Russell diagrams for our sample of objects towards N 11, NGC 2004, NGC 346 and NGC 330. Be objects are plotted as squares and objects showing evidence of binarity are plotted as open symbols. Non-rotating evolutionary tracks have been obtained from Meynet et al. (1994) and Schaerer et al. (1993) for the LMC objects and from Meynet et al. and Charbonnel et al. (1993) for the SMC objects. The dashed line indicates the magnitude limit for our observations in each region. It should be noted that many of the objects in each sample lie in overlapping positions in these figures.

observed, that for the main-sequence objects is unexpected. Although the scatter is large, given the number of objects, there may be a systematic difference. If it is assumed that no mass discrepancy should exist for main-sequence objects since this evolutionary stage is thought to be well understood, that observed could be due to binarity, errors in the distance estimate, bolometric corrections, reddening values or even the derived surface gravities. However, given that the magnitude of the effect is different in the SMC compared to the LMC, it is unlikely to be due to the derived gravities, or bolometric corrections as the same methodologies were used for each. Additionally the mass discrepancies for the binary systems are almost identical to those in Table 8 indicating that undetected binary systems are unlikely to be the cause of the discrepancies. Since the reddening values are small, the discrepancy may come from the distance estimates.

Using the evolutionary masses and atmospheric parameters listed in Tables 3-6, we have derived luminosity es-

Table 8. Mean mass-discrepancies for the sample of **single B-type stars. Objects are classified by surface gravity with supergiants having gravities less than 3.2 dex (see Sect. 5.1), giants between 3.2 and 3.7 dex and dwarfs greater than 3.7 dex.** Errors are the standard deviations and the value in brackets indicates the number of objects.

	$\log(M_{\text{evolutionary}}/M_{\text{spectroscopic}})$	
	LMC	SMC
Supergiants	0.17 ± 0.17 (22)	0.25 ± 0.19 (13)
Giants	0.06 ± 0.14 (43)	0.18 ± 0.14 (39)
Dwarfs	-0.14 ± 0.22 (51)	-0.05 ± 0.17 (60)

timates. It should be noted that these are different from

the luminosities listed in Tables 3-6, which assumed a fixed distance to each Cloud. Adopting the same reddenings and bolometric corrections as discussed in Sect. 3.7, it is then possible to derive distance estimates towards each star. For objects with $\log g \geq 3.7$ dex the mean distance moduli to the LMC and SMC are 18.16 ± 0.77 and 18.79 ± 0.55 from 51 and 60 objects respectively, where the uncertainties are the 1σ standard deviations, compared with our adopted values of 18.56 and 18.91. Although the mean value for the LMC is 0.4 dex smaller than that adopted in Sect. 3.7, it lies within the range of those reported for the LMC in the recent literature. For example, Udalski (1998) estimates a distance modulus of 18.13 for the LMC. However, it should also be noted that Udalski similarly estimates a distance modulus of 18.63 dex for the SMC which is 0.17 dex closer than our derived value of 18.80 dex and **0.28 dex closer than our adopted value of 18.91 dex. Excluding the most massive stars (greater than $25 M_{\odot}$) increases the mass discrepancies although within the uncertainties this is not significant.** To maintain consistency with published work from the FLAMES project the distance estimates discussed in Sect. 3.7 have been adopted throughout the subsequent discussion.

If corrections are applied to remove the mass discrepancy of the dwarf stars it further enhances the mass discrepancy of the evolved objects. However, such corrections result in similar mass discrepancies for the LMC and SMC evolved samples. This may indicate that the post-main-sequence evolution of massive stars is not fully understood and as discussed above, such mass discrepancies have previously been observed. In Sect. 5.1 several inconsistencies between the observations and the theoretical predictions of evolved objects are highlighted. In particular, we argue for extension of the hydrogen burning phase of the evolutionary tracks which would result in lower evolutionary masses being derived, hence reducing the mass discrepancy for evolved stars.

4. Populations within the sample

Atmospheric parameters and rotational velocities have been derived for a large sample of objects which contains several groups with different properties. In this section we compare these various subsets using as a control sample single, core hydrogen burning stars of less than $25 M_{\odot}$. In Sect. 5 we discuss how the subsets can be utilised to answer the three questions listed in Sect. 1.

4.1. High mass stars

Mass-loss rates generally increase with stellar mass (Maeder & Meynet 2001) and hence more massive objects should lose more angular momentum and rotate slower than less massive objects for a given initial rotational velocity. The theoretical evolutionary tracks of Maeder & Meynet show that mass-loss effects become significant for masses greater than $25 M_{\odot}$. In Table 9 we compare the mean projected rotational velocity for stars with masses greater than $25 M_{\odot}$ and those with masses of $\leq 25 M_{\odot}$. There is indeed some evidence that the more massive stars rotate slower, although it should be stressed that the number of objects with masses greater than $25 M_{\odot}$ is **only 7% of the sample** and the trend may not be statistically significant.

Table 9. Mean projected rotational velocities for **single core-hydrogen burning stars** with masses greater than $25 M_{\odot}$ and masses of $\leq 25 M_{\odot}$ in each region. Values in brackets indicate the number of stars in each sample.

Region	Mean $v \sin i$ (km s^{-1})			
	$M \leq 25 M_{\odot}$		$M > 25 M_{\odot}$	
NGC 346	150	(65)	113	(5)
NGC 330	154	(77)	73	(1)
N 11	149	(34)	126	(12)
NGC 2004	121	(60)	–	(0)

4.2. Binarity

Binarity effects can significantly alter the evolution of massive stars. For example, mass-transfer can lead to spin-up of the accreting star, while tidal interaction in close binary systems can lead to reduced rotational velocities through partial or full synchronisation of the rotational velocity with the orbital velocity (see for example Huang & Gies 2006; Abt et al. 2002; Zahn 1977). Indeed both Zahn (1994) and Hunter et al. (2007) find that massive stars in binary systems typically have smaller amounts of core processed material in their photosphere compared to single stars. This is consistent with tidal interaction reducing the rotational velocities and hence suppressing the rotational mixing of the products of nucleosynthesis into the photosphere.

Table 10. Mean projected rotational velocities of the **core hydrogen burning single and binary stars less massive than $25 M_{\odot}$ in each region. The binary population includes both single and double lined spectroscopic binaries.** Values in brackets indicate the number of stars in each sample.

Region	Mean $v \sin i$ (km s^{-1})			
	Single stars		Binary stars	
NGC 346	147	(67)	103	(25)
NGC 330	146	(83)	121	(8)
N 11	143	(35)	92	(30)
NGC 2004	120	(62)	99	(28)

In Table 10 the mean projected rotational velocities of single and binary stars are compared. It can be seen that binaries tend to have lower rotational velocities than single stars. This may indicate that tidal forces do play an important part in reducing the rotational velocities of massive stars. However, it is important to consider selection effects. Radial velocity variations (the evidence of binarity) are detected by cross-correlating individual exposures of the same wavelength region observed at different epochs to look for radial velocity shifts (Sect. 2.1). Such shifts are relatively simple to detect to a few km s^{-1} for stars with projected rotational velocities up to 100 km s^{-1} as the absorption lines are typically sharp and well defined. For stars with broad absorption lines and hence large projected rotational velocities, it is difficult to define the position of the core of the line and small radial velocity shifts will remain undetected. Additionally in binary

Table 11. Mean projected rotational velocities of the single supergiant (**surface gravities of less than 3.2 dex**) and core hydrogen burning stars with masses $\leq 25 M_{\odot}$. Values in brackets indicate the number of stars in each sample. Note that as upper limits are included in the supergiant sample, the means given here should be treated as upper limits to this class of object.

Region	Mean $v \sin i$ (km s^{-1})			
	Supergiants		Core hydrogen burning stars	
NGC 346	72	(1)	147	(67)
NGC 330	38	(12)	146	(83)
N 11	60	(11)	143	(35)
NGC 2004	60	(8)	119	(62)

systems with small orbital periods, the separation between the objects would be smaller, the velocity shifts greater and tidal interaction would be more important than for longer period systems. As such the rotational velocity distributions of binary objects could be biased towards stars having low rotational velocities. Clearly further studies of the binary populations in young clusters are required.

4.3. Supergiants

In Table 11 the mean projected rotational velocities of the supergiant and core hydrogen burning objects are compared with supergiants being considered as objects with surface gravities less than 3.2 dex (see Sect. 5.1). Assuming that the inclination axes of our targets are randomly orientated the mean rotational velocities would be a factor of $4/\pi$ larger than the values quoted in Table 11. It is clear that supergiants have much lower rotational velocities than core hydrogen burning objects which is simply a consequence of their evolutionary status.

4.4. Be stars

It has recently been reported that Be stars typically have larger rotational velocities than B-type stars (Martayan et al. 2006, 2007). A significant number (17%) of the stars in the FLAMES survey have been classified as Be type objects and hence it is possible to compare the rotational velocities of normal B-type stars with those showing Be characteristics. In Table 12 we present the average projected rotational velocities of the B- and Be-type stars in each region.

It is apparent that on average Be-type stars have higher rotational velocities than normal B-type stars in agreement with the finding of Martayan et al. (2006, 2007), see also Fig. 3. Zorec et al. (2005) have shown that the Be phenomena normally occurs early in the core hydrogen burning phase. They also show that for the most massive stars the Be phenomena disappears during their main-sequence lifetimes and postulate that this is due to mass-loss causing a star to spin down.

Table 12 additionally shows that we have observed many more Be-type stars in the SMC than the LMC, again in agreement with Martayan et al. 2007. If B-type stars become Be-type stars because they reach the main-sequence

Table 12. Comparison of the mean projected rotational velocities of the single core hydrogen burning B- and Be-type stars with masses $\leq 25 M_{\odot}$ in each region. Values in brackets indicate the number of stars in each sample.

Region	Mean $v \sin i$ (km s^{-1})			
	B stars		Be stars	
NGC 346	115	(45)	213	(22)
NGC 330	128	(64)	207	(19)
N 11	134	(31)	215	(4)
NGC 2004	105	(51)	190	(11)

with sufficiently high angular momentum, this may indicate that at lower metallicity, massive stars tend to rotate faster and suffer a smaller amount of spin down.

5. Discussion

5.1. Constraints on evolutionary history

The surface gravity of an object is a good indicator of its evolutionary status, with the gravity decreasing as an object evolves from a dwarf, to a giant and then into a supergiant star. In Fig. 8 we plot the projected rotational velocity against surface gravity.

The distributions of rotational velocities shown in Fig. 8 appear bi-modal in the sense that for surface gravities of < 3.2 dex the projected rotational velocities are small, while at higher values the distribution is much broader. **We interpret this limit of 3.2 dex to be the end of the core hydrogen burning phase**, since after this point the stars rapidly expand to become slowly rotating, core helium burning objects, as represented by the late B-type objects in our sample with surface gravities of ~ 2.0 dex. **Hence we consider objects with surface gravities lower than 3.2 dex to be supergiants.** We note that the predicted position of the end of core hydrogen burning shown by the evolutionary tracks occurs at higher surface gravities than that implied by our observations and suggests that the predicted core hydrogen burning lifetime needs to be extended to lower surface gravities. It is however important to stress a caveat. If the mass-discrepancy discussed in Sect. 3.8.1 is not due to an error in the adopted distance moduli, but instead due to a systematic error in our estimated surface gravities then our targets would have surface gravities that are systematically ~ 0.1 dex higher.

A large population of the giants lie in the post-main-sequence gap when compared with the evolutionary tracks shown in Fig. 7. Due to their small evolutionary timescale, such objects would not normally be expected to be observed. A similar over abundance of post-main-sequence objects in the Galactic clusters NGC 3293 and NGC 4755 was observed in Paper III. Extension of the end of the main-sequence (for example, by increasing the efficiency of overshooting) would allow the evolutionary tracks to encompass this giant phase during the core hydrogen burning phase. This would then be consistent **with the** presence of such objects in our samples.

The theoretical predictions of Maeder & Meynet (2001) indicate that rotational velocities remain relatively constant during core hydrogen burning, decreasing by approx-

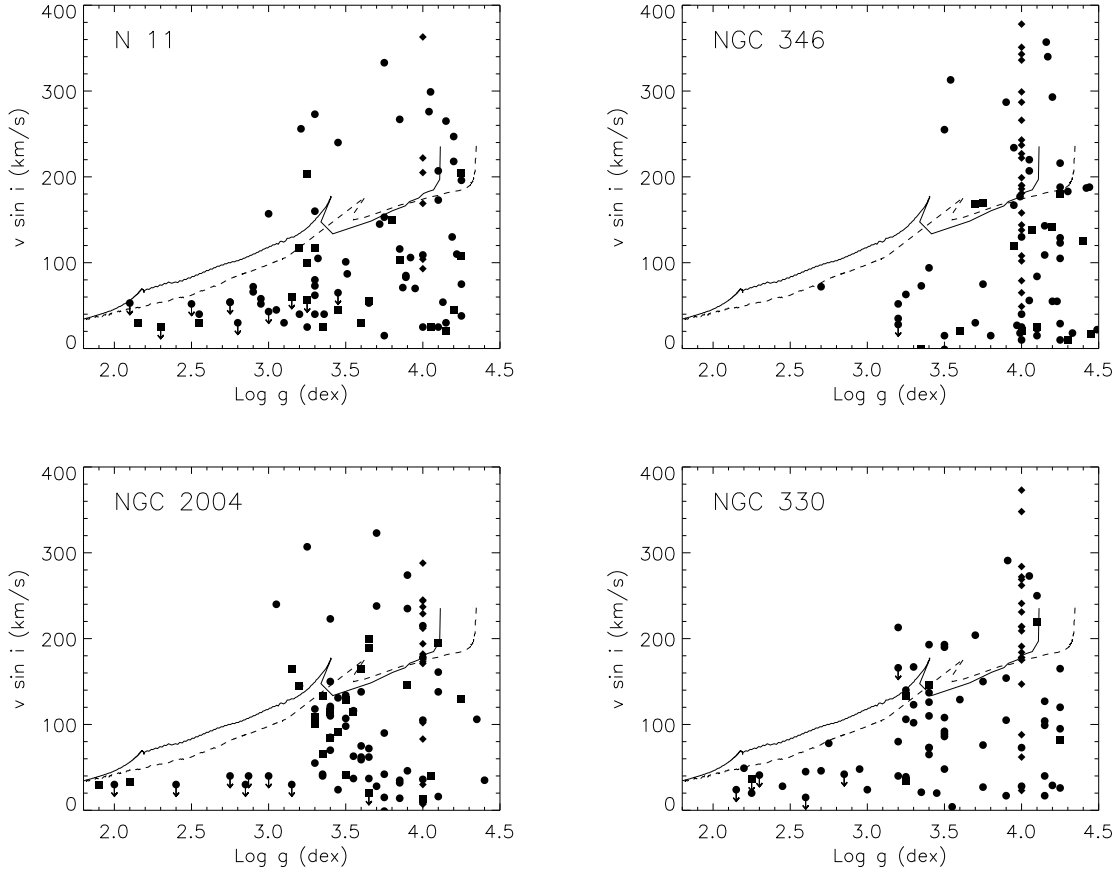


Fig. 8. Plots of projected rotational velocity ($v \sin i$) against the surface gravity for stars towards N11, NGC 2004, NGC 346 and NGC 330 showing the bi-modal distribution of rotational velocities. Be objects are assumed to be main-sequence objects with a surface gravity of 4.00 dex and are plotted as diamonds. Single lined spectroscopic binaries are indicated by square symbols. Downward arrows indicate upper limits to the $v \sin i$. The stellar evolutionary tracks of Maeder & Meynet (2001) for a $15 M_{\odot}$ star, with an initial rotational velocity of 300 km s^{-1} (scaled to take into account random angles of inclination) at SMC (dashed line) and Galactic (solid line) metallicity are shown.

imately 40 km s^{-1} from the zero-age main-sequence to the end of hydrogen burning. From Fig. 8 there may be some evidence that the objects with the largest surface gravities cover the widest range of rotational velocities **and indeed objects classified as giants have rotational velocities that are lower than those of dwarfs by on average $\sim 50 \text{ km s}^{-1}$ for our entire sample.** This appears to be consistent with giants being in the core hydrogen burning phase, again implying that extension of the evolutionary tracks may be necessary.

The evolutionary tracks of Maeder & Meynet (2001) which incorporate rotation show that for a $15 M_{\odot}$ star it takes $\sim 13.6 \text{ Myr}$ to reach the end of the hydrogen burning main-sequence, while the blue supergiant phase has a lifetime of less than 0.1 Myr , **i.e. the blue supergiant phase is less than 1% of the core hydrogen burning lifetime. The large number of supergiants observed in the FLAMES survey is unexpected with the ratio of supergiants to core hydrogen burning objects being $\sim 11\%$.** Significant populations of objects in the post-main-sequence gap have previously been seen (see, for example, Caloi et al. 1993; Fitzpatrick & Garmany 1990). However, it should be noted that the FLAMES survey preferentially se-

lected the brightest objects towards each cluster, and hence there may be some bias towards selecting supergiants.

The evolutionary tracks shown in Fig. 8 imply that the rotational velocity slows down relatively smoothly as the star evolves to low surface gravities after the core hydrogen burning phase, although, **as discussed above**, this phase is almost instantaneous compared with the core hydrogen burning lifetime. However, observationally this trend is not seen; objects with surface gravities $< 3.2 \text{ dex}$ have relatively constant rotational velocities, which are smaller than predicted. A similar trend has previously been observed by Dufton et al. (2006b). However, as discussed by Hunter et al. (2007) and Trundle et al. (2007) many of the supergiant objects are highly enriched in nitrogen and show evidence of binarity, suggesting that a mass-transfer event may have occurred. As such, comparison with single star evolutionary tracks may not be valid. Indeed, rejuvenation through a mass-transfer event is one method of populating this short evolutionary stage and may reconcile the over-abundance of supergiants in our samples with the predicted lifetime of such an evolutionary stage from single star models.

An alternative explanation is the possibility of blue-loops, where the supergiant goes through a red-supergiant phase and then returns to higher effective temperatures.

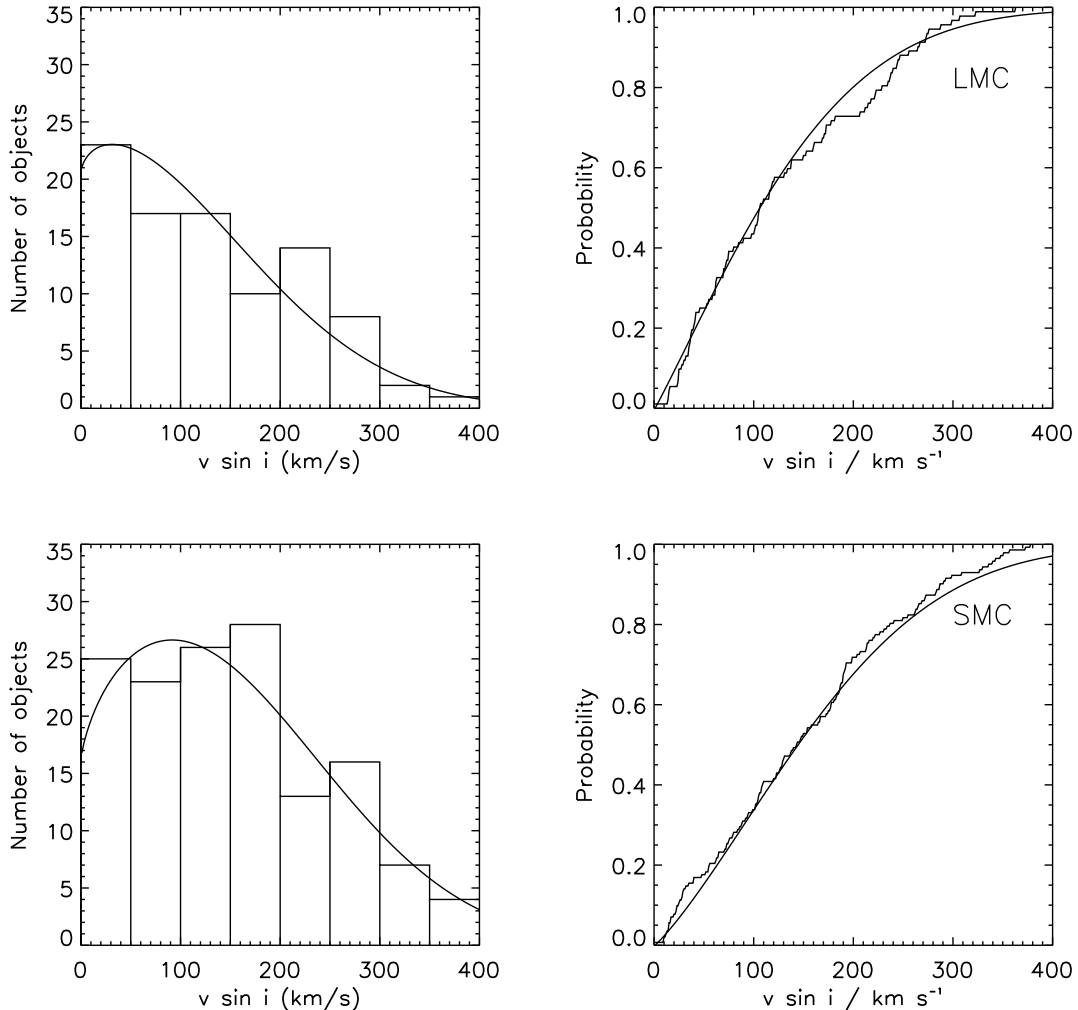


Fig. 9. Rotational velocity distributions of the single core-hydrogen burning LMC and SMC stars with masses $\leq 25 M_{\odot}$, upper and lower panels respectively. The LMC distribution is fitted with a intrinsic rotational velocity modelled by a Gaussian with a peak at 100 km s^{-1} and a $\frac{1}{e}$ half width, of 150 km s^{-1} , while the SMC distribution is fitted with a Gaussian having a peak at 175 km s^{-1} and a half-width of 150 km s^{-1} .

Such a process would lead to the observed nitrogen enhancements and rotational velocities and an increased lifetime in the blue supergiant phase although the blue-loop phase is not well constrained in the evolutionary models (G. Meynet and N. Langer, private communications). We therefore believe that the supergiant population of objects shown in Fig. 8 are not the result of direct single star evolution from the core hydrogen burning phase and either binarity or blue loops may be responsible for this supergiant population.

5.2. Rotation and metallicity

As discussed in Sect. 1, stars at low metallicity are predicted to rotate faster as they lose less angular momentum through their stellar winds and are generally more compact. Our sample of objects covers the metallicity regimes of the LMC and SMC and hence it is possible to look for metallicity effects. To increase our sample sizes we have combined together those for N 11 and NGC 2004 in the LMC

and NGC 346 and NGC 330 in the SMC sample. **Only single core hydrogen burning objects with masses of $\leq 25 M_{\odot}$ have been considered and this corresponds to 48% and 70% of our LMC and SMC samples respectively.** The upper limit in mass was set to minimise the possible effects due to mass-loss as discussed in Sect. 4.1, whilst the supergiants have been excluded as their rotational velocities will not be representative of their main-sequence progenitors. Our samples generally have spectral types between B0 and B3, and have initial masses between 7 and $25 M_{\odot}$. The spectral type distributions of both samples are similar and there is no reason to expect any trend of rotational velocity with spectral type over this small range.

In Fig. 9, the distribution of projected rotational velocities in the LMC and SMC are shown together with their cumulative probability functions. The number of objects we have observed should be sufficient to allow us to estimate the intrinsic rotational velocity distribution. Following the

procedures discussed in Paper III, we have attempted to fit these distributions with a Gaussian function convolved with a function to take into account random angles of inclination. A chi-squared test has been performed to obtain the best fit to the cumulative probability functions. We chose not to apply the chi-squared test to the fit to the histograms, as this may be dependent on the choice of binsize.

For the LMC sample, an intrinsic velocity distribution with a peak at 100 km s^{-1} and a $\frac{1}{e}$ half width of 150 km s^{-1} (which corresponds to a full-width-half-maximum, FWHM, of 250 km s^{-1}) **is found, with corresponding values for the SMC sample being 175 km s^{-1} and 150 km s^{-1} .** Although a Gaussian distribution has been assumed, as discussed in Paper III and in Mokiem et al. (2006) any function with a similar profile would also provide a satisfactory fit. For example as the Gaussian profiles are quite broad, a rectangular profile centred on the Gaussian peaks, with similar widths, would also give a reasonable fit to the observed distributions. From these results it appears that the LMC objects typically rotate significantly more slowly than those of the SMC. Indeed, the Student's t-test gives a 93% probability that the means of the two distributions are significantly different while the K-S statistical test gives the probability that the distributions are drawn from the same parent population to be less than 10%.

To further investigate metallicity effects the Magellanic Cloud samples can be compared with Galactic results. However before this is possible, it is necessary to ensure that the samples are comparable. For example, the Galactic objects observed in the FLAMES project and discussed in Paper III mostly lie within two cluster radii of their respective clusters. From the discussion in Sect. 2.3 it is apparent that the objects that we observed in the Magellanic Clouds lie much further from the centre of their respective associations. Our sample is therefore likely to be dominated by field or unbound objects and it may be more appropriate to compare the rotational velocity distributions discussed here with Galactic field stars, rather than the Galactic cluster stars discussed in Paper III. Indeed, it has been shown in Paper III and by Wolff et al. (2007) that the mean rotational velocities of Galactic cluster objects are higher than Galactic field stars. **For example, strong peaks in the Galactic cluster rotational velocity distributions occur at $\sim 200 \text{ km s}^{-1}$ while the field population discussed below peaks at $\sim 50 \text{ km s}^{-1}$.**

Abt et al. (2002) and Howarth et al. (1997) present rotational velocities for a large number of B-type and O-type stars in the Galactic field respectively. In order to maintain consistency between the Galactic and Magellanic Cloud samples we have randomly chosen Galactic objects from these catalogues in such a way as to populate an equivalent spectral type distribution as the Magellanic Cloud samples, with 198 objects being selected in total. In Fig. 10 cumulative probability functions are plotted for this Galactic sample and the LMC and SMC objects shown in Fig. 9. It is clear that the SMC objects typically rotate faster than the Galactic objects with the LMC distribution lying between the two. Given that we are randomly selecting Galactic comparison objects, we have carried out the comparison 1000 times. The Student's t-test and the K-S test give the probability that the Galactic and LMC samples are drawn from the same distribution to be 43% and 24% respectively from the mean of these 1000 comparisons. Similarly the

two tests show that the probability the Galactic and SMC samples are drawn from the same distribution of rotational velocities to be 0.3% and 0.8%. Hence while there is some evidence that the LMC sample of stars may rotate faster than those in the Galactic field, the faster rotation of the SMC B-type objects compared to the Galactic objects is significant at the 3σ level.

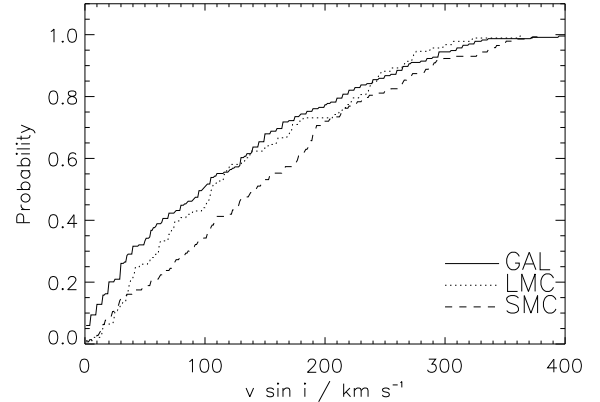


Fig. 10. Cumulative probability functions of the rotational velocities of the **single core-hydrogen burning LMC and SMC objects with masses $\leq 25 M_{\odot}$** . For comparison Galactic (GAL) objects from Howarth et al. (1997) and Abt et al. (2002) are included (see text). The median intrinsic rotational velocities are 125 , 135 and 183 km s^{-1} for the Galactic, LMC and SMC samples respectively (assuming random angles of inclination) **indicating a metallicity dependence.**

5.3. Implications for gamma-ray burst progenitors

The progenitors of long duration gamma-ray bursts (hereafter GRBs) have been suggested to be rapidly rotating massive carbon-oxygen stars that have lost their entire hydrogen and helium envelopes. This poses a problem for stellar evolutionary models in that one has to remove the outer envelope of a massive star, to create a Wolf-Rayet type object (WR), but maintain or enhance the rotational velocity (Woosley & Heger 2006).

Very rapidly rotating main-sequence stars have been proposed as candidates for chemically homogeneous evolution, in which the stars are homogeneously mixed on a timescale much shorter than their nuclear lifetimes (Maeder 1987; Langer 1992). In this case the star becomes a WR star directly by evolving to the blue, and its outer hydrogen envelope is effectively mixed into the star rather than being lost through stellar winds. This avoids angular momentum loss through mass-loss, and hence one can potentially get a viable GRB progenitor i.e. a massive CO star that is hydrogen and helium free and rapidly rotating (Yoon & Langer 2005, Woosley & Heger 2006). Our rotational velocity results, and the determination of a frequency distribution can provide a critical input parameter for these models.

Yoon et al. (2006) have recently generated massive star evolutionary models at SMC and lower metallicities to study the plausibility of chemically homogeneous evolution

generating GRB progenitors. They assumed a distribution function of rotational velocities which was estimated from the most massive O-type stars in our FLAMES survey data set. Mokiem et al. (2006) determined projected rotational velocities for the 17 unevolved O-stars in NGC 346 and estimated the intrinsic rotational velocity distributions, as in Sect. 5.2. Given the young age of NGC 346 it would be expected that angular momentum loss due to winds should be small and the current rotational velocity distribution should be representative of the initial rotational velocity distribution. In order to determine the rate of GRB production from rapidly rotating, chemically homogeneous stars, Yoon et al. (2006) then assumed that this rotational velocity distribution was **appropriate** to all masses and metallicities. They predict that at metallicities of $Z = 0.00001 - 0.001$ stars with initial masses as low as $11-14 M_{\odot}$ can produce GRBs. By combining our full FLAMES survey sample (Mokiem et al., and this paper) we have the most extensive rotational velocity survey at low metallicities to test these ideas.

As suggested by Table 9 the more massive stars may rotate slower than their less massive counterparts, implying a possible mass dependence. However, if mass-loss effects are small in the O-star sample whilst on the main-sequence, this effect may be due to mass and metallicity dependent protostellar winds rather than winds on the main-sequence (Yoon et al. 2006). In Fig. 11 we plot the cumulative probability function for the ratio of projected rotational velocity to critical (Keplerian) rotational velocity for the unevolved O-stars in the Mokiem et al. NGC 346 sample and compare this to that derived for the NGC 346 B-type stars here. There is a clear offset between the two distributions, with the B-stars having higher ratios of rotational to critical velocity. We note again that the mass range of the B-stars presented here are $10-25 M_{\odot}$, whereas the O-stars of Mokiem et al. have masses mostly in the range $20-60 M_{\odot}$. **This is the first time we have had enough objects to carry out this mass-dependent comparison. Hence the Yoon et al. rates of GRBs from rapidly rotating stars below $20 M_{\odot}$ (greater than $v \sin i / v_{\text{Kep}} \simeq 0.5$) are probably underestimates.**

It would be desirable to recalculate GRB rates with our new measurements of lower mass stellar rotational velocities. Yoon et al. (in their Fig. 3) calculate that stars of $30 M_{\odot}$ require a minimum rotational velocity of $v \sin i / v_{\text{Kep}} \sim 0.27$ to be viable GRB candidates, which from Fig. 11 is about 10-15% of the O-type stellar population. A $14 M_{\odot}$ star however requires a minimum rotational velocity of $v \sin i / v_{\text{Kep}} \sim 0.43$, suggesting about 15% of that population could be viable GRB progenitors. Given the similarity of these percentages, the initial mass function should imply more progenitors from the lower mass range. **We therefore suggest that adopting our observed rotational velocity for the full mass range will increase the fraction of stars which become GRBs. A quantitative estimate requires a detailed grid calculation as in Yoon et al. This is outside the scope of this paper but it should be done with the complete rotational velocity distribution that we present here.**

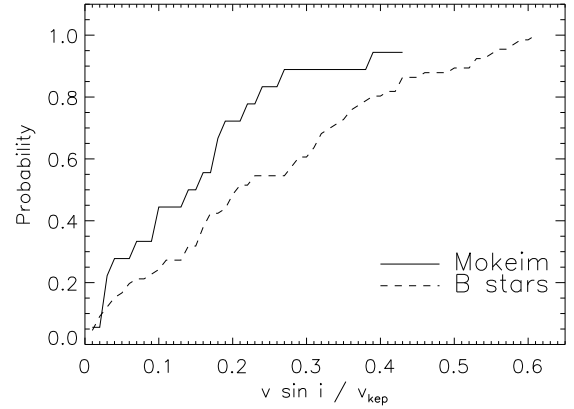


Fig. 11. Cumulative probability functions of projected rotational velocity to critical rotational velocity ratio for the unevolved NGC 346 O-star sample from Mokiem et al. (2006, Mokiem) and our **single core-hydrogen burning** NGC 346 B-type star sample. **This plot shows that the rotational velocity distribution of the more massive O-stars is peaked towards lower rotational velocities than that of the B-type stars.**

6. Conclusions

Atmospheric parameters and projected rotational velocities are presented for approximately 400 O- and early B-type stars towards four clusters in the Magellanic Clouds, which combines this work, the analysis of some 50 O-type stars (Mokiem et al. 2006, 2007) and the analysis of 100 narrow lined B-type stars (Hunter et al. 2007 and Trundle et al. 2007). This represents the full data set from our ESO Large Programme, the VLT Flames survey of massive stars in the Magellanic clouds and the Galaxy. **From the subsets of the data we find that supergiants are the slowest rotators in the sample, typically having rotational velocities less than 80 km s^{-1} . Additionally binaries tend to rotate slower than single objects, but given that binarity is easier to detect at low projected rotational velocities this result may be dominated by selection effects. It is also found that objects with Be phenomena are typically the fastest rotators in our dataset, which is in agreement with previous studies. The number of high mass objects ($M > 25 M_{\odot}$) in the combined sample is limited but there is some evidence that the most massive objects rotate slower than their less massive counterparts. We utilise the single core-hydrogen burning objects along with these subsets to address the questions outlined in Sect. 1.**

- Current evolutionary models do not predict the large number of giants observed in our samples which may imply that the theoretical tracks need to be extended. Indeed we find that stars classed as giants typically rotate some $\sim 50 \text{ km s}^{-1}$ slower than dwarf objects and this is consistent with a modest slowing down of the rotational velocity over the core hydrogen burning lifetime, indicating that giants are still in the hydrogen burning phase. From the bi-model distribution of rotational velocities for supergiant and core-

Table 13. Peak and width of the Magellanic Cloud rotational velocity distributions determined by fitting the distributions with a Gaussian function, see Sect. 5.2.

Region	Peak km s^{-1}	$\frac{1}{e}$ half-width km s^{-1}
LMC	100	150
SMC	175	150

hydrogen burning objects we observe the end of the core-hydrogen burning phase to be at 3.2 dex. We also show that supergiants are unlikely to have evolved directly from the hydrogen burning main-sequence, but instead, binarity or blue loops may be a more likely explanation for the observed supergiant population.

- Our sample is dominated by field objects and we compare the rotational velocity distributions with Galactic field objects from the literature, finding that the SMC metallicity stars rotate fastest, in agreement with theoretical predictions. The difference between the SMC stars and Galactic field stars is significant at the 3σ level, suggesting we have detected a real difference. However we find no significant difference between the rotational velocity distributions of the Galactic and LMC stars. By assuming random angles of inclination, we can model the observed $v \sin i$ distributions with broad Gaussians with the parameters listed in Table 13.
- **Objects more massive than $25 M_{\odot}$ tend to rotate slower than less massive objects and this could be due to mass-loss effects, with a very massive star losing angular momentum through strong stellar winds, although this is unexpected in the SMC. An alternative explanation is that the initial birth rotational velocity is mass dependent, perhaps due to protostellar winds. However, the consequence is that Yoon et al. (2006) may have underestimated the rotational velocity distribution of 10-20 M_{\odot} GRB progenitors.** We therefore suggest that the rotational velocity distribution derived here should be employed in future GRB rate calculations, and this may even increase the rate of GRBs expected at low metallicity due to the greater prevalence of B-type stars.

Acknowledgements. We are grateful to staff from the European Southern Observatory for assistance in obtaining the data. This work, conducted as part of the award ‘Understanding the lives of massive stars from birth to supernovae’ (SJS) made under the European Heads of Research Councils and European Science Foundation EURYI (European Young Investigator) Awards scheme, was supported by funds from the Participating Organisations of EURYI and the EC Sixth Framework Programme. SJS also acknowledges the Leverhulme Trust. Additionally we acknowledge support from PPARC (UK Particle Physics and Astronomy Research Council) and DEL (Dept. of Employment & Learning Northern Ireland).

References

- Abt, H.A., Levato, H., Grosso, M. 2002, ApJ, 573, 359
Balona, L. 1994, MNRAS, 268, 119
Bastian, N. & Gieles, M. 2006, ‘Cluster Disruption: Combining Theory and Observations’, to appear in the ASP conference proceedings, astro-ph/0609669
Bouchet, P., Lequeux, J., Maurice, E., Prevot, L. & Prevot-Burnichon, M.L. 1985, A&A, 149, 330
Bouret, J.-C., Lanz, T., Hillier, D.J., et al. 2003, ApJ, 595, 1182
Caloi, V., Cassatella, A., Castellani, V., & Walker, A. 1993, A&A, 271, 109
Charbonnel, C., Meyent, G., Maeder, A., Schaller, G. & Schaerer, D. 1993, A&AS, 101, 415
Conti, P.S. & Ebbets, D. 1977, ApJ, 213, 438
Dufton, P.L., Ryans, R.S.I., Simón-Díaz, S., Trundle, C. & Lennon, D. J. 2006b, A&A, 451, 603
Dufton, P.L., Ryans, R.S.I, Trundle, C., et al. 2005, A&A, 434, 1125
Dufton, P.L., Smartt, S.J., Lee, J.-K., et al. 2006, A&A, 457, 265 (Paper III)
Evans, C.J., Lennon, D.J., Smartt, S.J., & Trundle, C. 2006, A&A, 456, 632 (Paper II)
Evans, C.J., Smartt, S.J., Lee, J.-K., et al. 2005, A&A, 437, 467 (Paper I)
Fitzpatrick, E.L. & Garmany, C.D. 1990, ApJ, 363, 119
Frémat, Y., Zorec, J., Hubert, A.-M. & Floquet, M. 2005, A&A, 440, 305
Gieren, W., Storm, J., Barnes, T.G. III, Fouqué, P., Pietrzyński, G. & Kienzle, F. 2005, ApJ, 627, 224
Gies, D.R. & Lambert, D.L. 1992, ApJ, 387, 673
Gonzalez, G. & Wallerstein, G. 1999, AJ, 117, 2286
Goodwin, S.P. & Bastian, B. 2006, MNRAS, 373, 752
Gouliermis, D.A., Dolphin, A.E., Brandner, W. & Henning, Th. 2006, ApJS, 166, 549
Gray, D.F. 1976, The observation and analysis of stellar photospheres. Cambridge Univ. Press, Cambridge
Heger, A. & Langer, N. 2000, ApJ, 544, 1016
Herrero, A., Kudritzki, R.P., Vilchez, J.M., et al. 1992, A&A, 261, 209
Hilditch, R.W., Howarth, I.D. & Harries, T.J. 2005, MNRAS, 357, 304
Howarth, I.D., Siebert, K.W., Hussain, G.A.J., Prinja, R.K. 1997, MNRAS, 284, 265
Huang, W. & Gies, D.R. 2006, ApJ, 648, 591
Hubeny, I. & Lanz, T. 1995, ApJ, 439, 875
Hunter, I., Dufton, P.L., Smartt, S.J. et al. 2007, A&A, 466, 277
Keller, S.C. 2004, PASA, 21, 310
Korn, A.J., Keller, S.C., Kaufer, A. et al. 2002, A&A, 385, 143
Korn, A.J., Nieva, M.F., Daflon, S. & Cunha, K. 2005, ApJ, 633, 899
Kudritzki, R.-P., Pauldrach A. & Puls J. 1987, A&A, 173, 293
Kudritzki R.P. & Puls J. 2000, ARA&A, 38, 613
Langer N., 1992, A&A, 265, L17
Lennon, D.J., Dufton, P.L. & Crowley, C. 2003, A&A, 317, 87
Lennon, D.J., Lee, J.-K., Dufton, P.L. & Ryans, R.S.I. 2005, A&A, 438, 265
Maeder, A., 1987, A&A, 178, 159
Maeder, A. & Meynet, G. 2001, A&A, 373, 555
Martayan, C., Frémat, Y., Hubert, A.-M., Floquet, M., Zorec, J. & Neiner, C. 2007, A&A, 462, 683
Martayan, C., Frémat, Y., Hubert, A.-M., Floquet, M., Zorec, J. & Neiner, C. 2006, A&A, 452, 273
Massey, P., Lang, C.C., Degioia-Eastwood, K. & Garmany, C.D. 1995, ApJ, 438, 188
Massey, P., Parker, J.W. & Garmany, C.D. 1989, ApJ, 98, 1305
Meynet, G. & Maeder, A. 2000, A&A, 361, 101
Meynet, G., Maeder, A., Schaller, G., Schaerer, D. & Charbonnel, C. 1994, A&AS, 103, 97
Mokiem, M.R., de Koter, A., Evans, C.J., et al. 2007, A&A, 465, 1003
Mokiem, M.R., de Koter, A., Evans, C.J., et al. 2006, A&A, 456, 1131
Penny, L.R. 1996, ApJ, 463, 737
Ryans, R.S.I, Dufton, P.L., Rolleston, W.R.J., et al. 2002, MNRAS, 336, 577
Sagar, R. & Richtler, T. 1991, A&A, 250, 324
Schaerer, D., Meyent, G., Maeder, A. & Schaller, G. 1993, A&AS, 98, 523
Simón-Díaz, S. & Herrero, A. 2007, A&A, in press, astro-ph/0703216
Sirianni, M., Nota, A., de Marchi, G., Leitherer, C. & Clampin, M. 2002, ApJ, 579, 275
Slettebak, A., Collins, G.W. II, Parkinson, T.D., Boyce, P.B., & White, N.M. 1975, ApJS, 29, 137
Slettebak, A. 1956, ApJ, 124, 173
Smiljanic, R., Barbury, B., De Medeiros, J.R., & Maeder, A. 2006, A&A, 449, 655
Strom, S.E., Wolff, S.C. & Dror, D.H.A. 2005, ApJ, 129, 809
Townsend, R.H.D., Owocki, S.P. & Howarth, I.D. 2004, MNRAS, 350, 189
Trundle, C., Dufton, P.L., Hunter, I., et al. 2007, A&A, 471, 625

- Trundle, C. & Lennon, D.J. 2005, *A&A*, 434, 677
Udalski, A. 1998, *AcA*, 48, 113
Vacca, W.D., Garmany, C.D. & Shull, M.J. 1996, *ApJ*, 460, 914
Venn, K.A. 1999, *ApJ*, 518, 405
Vink, J.S., de Koter, A. & Lamers, H.J.G.L.M. 2001, *A&A*, 369, 574
Voels. S.A., Bohannan, B., Abbot, D.C. & Hummer, D.G. 1989, *ApJ*, 340, 1073
von Zeipel, H. 1924, *MNRAS*, 84, 684
Wolff, S.C, Strom, S.E. & Dror, D. 2007, *AJ*, 133, 1092
Woosley, S.E. & Heger, A., in *Gamma Ray Bursts in the Swift Era*, eds. S. S. Holt, N. Gehrels and J. Nousek, *AIP Conf.*, 2006, astro-ph/0604131
Woosley, S.E. & Heger, A., 2006, *ApJ*, 637, 914
Yoon, S.-C., Langer, N. & Norman, C. 2006, *A&A*, 460, 199
Yoon, S.-C., Langer, 2005, *A&A*, 443, 643
Zahn, J.-P. 1994, *A&A*, 288, 829
Zahn, J.-P. 1977, *A&A*, 57, 383
Zorec, J., Fremat, Y. & Cidale, L. 2005, *A&A*, 441, 235

Table 1. Radial distances (r_{rad} , arcmins) of the objects in the NGC 346 FLAMES sample with respect to the centre of star formation taken as the position of object 435 from the Massey et al. (1989) catalogue of OB stars in NGC 346; $\alpha = 00\ 59\ 04.49$ $\delta = -72\ 10\ 24.7$. The centre of NGC 346 adopted in Paper II for calculation of radial distances was obtained from the SIMBAD database (operated at the CDS, Strasbourg, France) and is actually the centre of the ionised shell of gas, which is offset from the cluster centre.

Object	r_{rad}	Object	r_{rad}	Object	r_{rad}	Object	r_{rad}
NGC 346-001	2.13	NGC 346-030	4.27	NGC 346-059	5.53	NGC 346-088	6.69
NGC 346-002	5.55	NGC 346-031	7.01	NGC 346-060	4.75	NGC 346-089	8.07
NGC 346-003	3.36	NGC 346-032	5.83	NGC 346-061	5.68	NGC 346-090	5.09
NGC 346-004	7.22	NGC 346-033	0.71	NGC 346-062	6.61	NGC 346-091	8.68
NGC 346-005	8.49	NGC 346-034	0.44	NGC 346-063	5.69	NGC 346-092	4.14
NGC 346-006	5.69	NGC 346-035	5.84	NGC 346-064	5.44	NGC 346-093	0.74
NGC 346-007	0.56	NGC 346-036	2.15	NGC 346-065	1.88	NGC 346-094	5.28
NGC 346-008	5.74	NGC 346-037	4.07	NGC 346-066	1.86	NGC 346-095	8.43
NGC 346-009	3.74	NGC 346-038	5.34	NGC 346-067	6.19	NGC 346-096	8.38
NGC 346-010	6.88	NGC 346-039	8.60	NGC 346-068	5.60	NGC 346-097	0.86
NGC 346-011	9.17	NGC 346-040	3.46	NGC 346-069	9.43	NGC 346-098	2.70
NGC 346-012	4.82	NGC 346-041	8.42	NGC 346-070	3.56	NGC 346-099	8.63
NGC 346-013	2.34	NGC 346-042	8.39	NGC 346-071	7.85	NGC 346-100	6.89
NGC 346-014	4.99	NGC 346-043	4.02	NGC 346-072	3.32	NGC 346-101	4.96
NGC 346-015	8.47	NGC 346-044	3.25	NGC 346-073	7.21	NGC 346-102	5.34
NGC 346-016	6.04	NGC 346-045	3.89	NGC 346-074	8.30	NGC 346-103	7.54
NGC 346-017	7.54	NGC 346-046	3.80	NGC 346-075	4.68	NGC 346-104	1.19
NGC 346-018	2.93	NGC 346-047	9.35	NGC 346-076	1.88	NGC 346-105	3.50
NGC 346-019	2.37	NGC 346-048	2.55	NGC 346-077	1.31	NGC 346-106	7.49
NGC 346-020	6.41	NGC 346-049	7.70	NGC 346-078	5.43	NGC 346-107	0.45
NGC 346-021	4.58	NGC 346-050	1.48	NGC 346-079	0.34	NGC 346-108	4.59
NGC 346-022	1.32	NGC 346-051	0.37	NGC 346-080	1.14	NGC 346-109	6.03
NGC 346-023	1.94	NGC 346-052	6.93	NGC 346-081	5.61	NGC 346-110	5.91
NGC 346-024	2.67	NGC 346-053	7.60	NGC 346-082	5.78	NGC 346-111	0.49
NGC 346-025	3.73	NGC 346-054	2.88	NGC 346-083	1.83	NGC 346-112	1.76
NGC 346-026	3.87	NGC 346-055	3.20	NGC 346-084	5.88	NGC 346-113	4.10
NGC 346-027	3.12	NGC 346-056	1.06	NGC 346-085	6.63	NGC 346-114	5.16
NGC 346-028	2.56	NGC 346-057	5.38	NGC 346-086	0.20	NGC 346-115	0.11
NGC 346-029	1.76	NGC 346-058	3.40	NGC 346-087	6.19	NGC 346-116	6.26

Table 3. Atmospheric parameters and $v \sin i$ values for the NGC 346 sample. In the method column, M06, T06 or H06 indicates that the values have been directly obtained from Mokiem et al. (2006, 2007), Trundle et al. (2007) or Hunter et al. (2007). He indicates the methodology outlined in Sect. 3.2 has been used to derived the atmospheric parameters. ‘A’ indicates that the temperature has been assumed based on spectral type. Values marked with colons indicate parameters where fitting has been difficult and the uncertainties may be larger than normal. Where it was possible to measure the projected rotational velocity of the secondary object in a double lined spectroscopic binary system, a second entry is given with ‘B’ appended to the object identifier. We do not give atmospheric parameters for those objects listed as Be stars (Be), double lined spectroscopic binaries (SB2) or classified with an uncertain spectral type (SP?).

Star	Spectral Type	T_{eff} (K)	$\log g$ (dex)	$v \sin i$ (km s^{-1})	Method	L/L_{\odot}	Mass (M_{\odot})	Comments
NGC 346-001	O7 Iaf+	34100	3.35	74	M06	6.02	66	Binary
NGC 346-004	Be(B1:)	Be	–	266	–	5.17	23	
NGC 346-007	O4 V((f+))	42800	3.95	120	M06	5.45	40	Binary
NGC 346-008	B1e	Be	–	299	–	4.96	20	
NGC 346-009	B0e	Be	–	199	–	5.08	24	
NGC 346-010	O7 IIIIn((f))	35900	3.54	313	M06	5.20	27	
NGC 346-012	B1 Ib	24200	3.20	<28	H06	4.77	16	
NGC 346-013	B1:	SB2	–	120	–	4.79	17	Binary
NGC 346-013B		SB2	–	320	–			Binary
NGC 346-015	B1 V	SB2	–	45	–	4.79	17	Binary
NGC 346-015B		SB2	–	35	–			Binary
NGC 346-016	B0.5 Vn	SB2	–	181	–	4.87	19	Binary
NGC 346-018	O9.5 IIIe	32700	3.33	138	M06	5.10	24	
NGC 346-020	B1 V+earlyB	SB2	–	34	–	4.69	16	Binary
NGC 346-020B		SB2	–	66	–			Binary
NGC 346-021	B1 III	25150	3.50	15	H06	4.61	14	
NGC 346-022	O9 V	36800	4.20	55	M06	4.95	24	
NGC 346-023	B0.2:(Be-Fe)	Be	–	65	–	4.81	18	
NGC 346-024	B2:shell(Be-Fe)	Be	–	190	–	4.59	19	
NGC 346-025	O9V	36200	4.07	138	M06	4.90	23	Binary
NGC 346-026	B0 IV (Nstr)	32500	3.75	75	He	4.85	20	
NGC 346-027	B0.5 V	31000	4.05	220	He	4.78	18	
NGC 346-028	OC6 Vz	42900	3.97	27	M06	5.10	32	
NGC 346-029	B0 V	32150	4.10	25	H06	4.82	19	Binary
NGC 346-030	B0 V	SB2	–	183	–	4.81	19	Binary
NGC 346-031	O8 Vz	39500	3.99	18	M06	4.99	27	
NGC 346-032	B0.5 V	29000	4.40	125	He	4.68	17	Binary
NGC 346-033	O8 V	39900	4.44	188	M06	4.99	27	
NGC 346-035	B1 V	SB2	–	145	–	4.61	15	Binary
NGC 346-035B		SB2	–	105	–			Binary
NGC 346-036	B0.5 V(Be-Fe)	Be	–	287	–	4.69	17	
NGC 346-037	B3 III	18800	3.20	35	H06	4.21	10	
NGC 346-039	B0.7 V	25800	3.60	20	H06	4.51	13	Binary
NGC 346-040	B0.2 V	30600	4.00	20	H06	4.67	17	Binary
NGC 346-041	B2 (Be-Fe)	Be	–	144	–	4.46	12	
NGC 346-043	B0 V	33000	4.25	10	H06	4.71	18	
NGC 346-044	B1 II	23000	3.50	40	H06	4.33	11	
NGC 346-045	B0.5 Vne	Be	–	181	–	4.56	15	
NGC 346-046	O7 Vn	39700	4.17	340	M06	4.81	24	
NGC 346-047	B2.5 III	19850	3.25	63	A	4.15	10	
NGC 346-048	Be (B3 shell)	Be	–	158	–	4.15	10	
NGC 346-049	B8 II	13000	2.70	80	He	3.70	7	
NGC 346-050	O8 Vn	37200	4.16	357	M06	4.67	21	
NGC 346-051	O7 Vz	41600	4.33	18	M06	4.87	27	
NGC 346-052	B1.5 V	SB2?	–	12	–	4.37	12	Binary?
NGC 346-053	B0.5 V	29500	3.75	170	He	4.51	15	Binary
NGC 346-054	B1 V	27300	4.20	23	A	4.41	13	
NGC 346-055	B0.5 V	29500	4.00	130	He	4.49	15	
NGC 346-056	B0 V	31000	3.80	15	H06	4.55	16	

Table 3. -continued.

Star	Spectral Type	T_{eff} (K)	$\log g$ (dex)	$v \sin i$ (km s^{-1})	Method	L/L_{\odot}	Mass (M_{\odot})	Comments
NGC 346-057	B2.5 III	19850	3.35	73	A	4.09	9	
NGC 346-058	B0.5 V	29500	4.25	180	He	4.47	14	Binary
NGC 346-061	B1-2 (Be-Fe)	Be	–	336	–	4.32	12	
NGC 346-062	B0.2 V	29750	4.00	25	H06	4.45	15	
NGC 346-064	B1-2 (Be-Fe)	Be	–	108	–	4.31	12	
NGC 346-065	B3 (Be-Fe)	Be	–	222	–	4.05	9	
NGC 346-066	O9.5 V	35600	4.25	129	M06	4.59	19	
NGC 346-067	B1-2 (Be-Fe)	Be	–	351	–	4.29	12	
NGC 346-068	B0 V (Be-Fe)	Be	–	378	–	4.51	16	
NGC 346-069	B1-2 (Be-Fe)	Be	–	186	–	4.28	12	
NGC 346-070	B0.5 V	30500	4.15	109	He	4.43	15	
NGC 346-072	B1-2 (Be-Fe)	Be	–	102	–	4.26	12	
NGC 346-073	B1-2 (Be-Fe)	Be	–	190	–	4.26	12	
NGC 346-074	B3 III	16500	3.20	52	He	3.80	7	
NGC 346-075	B1 V	27700	4.30	10	H06	4.31	13	Binary
NGC 346-076	B2 (Be-Fe)	Be	–	237	–	4.21	11	
NGC 346-077	O9 V	36500	3.99	177	M06	4.65	20	
NGC 346-078	B2 III	SB2?	–	154	A	4.05	9	Binary?
NGC 346-079	B0.5 Vn	29500	4.20	293	He	4.37	14	
NGC 346-080	B1 V	27300	4.25	216	A	4.29	12	
NGC 346-081	B2 IIIIn	21200	3.50	255	A	4.03	9	
NGC 346-082	B2 III	21200	3.70	168	A	4.03	9	Binary
NGC 346-083	B1 V	27300	4.05	207	A	4.28	12	
NGC 346-084	B1 V	27300	4.25:	105	A	4.27	12	
NGC 346-085	B2 III	SB2	–	26	–	4.03	9	Binary
NGC 346-085B		SB2	–	11	–	–	–	Binary
NGC 346-088	B1 V	27300	4.10:	84	A	4.26	12	
NGC 346-089	B1-2 (Be-Fe)	Be	–	79	–	4.21	11	
NGC 346-090	O9.5 V	34900	4.25	188	M06	4.56	18	
NGC 346-091	B1e	Be	–	49	–	4.25	12	Binary
NGC 346-092	B1 Vn	27300	3.95	234	A	4.24	12	
NGC 346-093	B0 V	34400	4.42	187	M06	4.53	18	
NGC 346-094	B0.7 V	28500	4.00	40	H06	4.28	13	
NGC 346-095	B1-2 (Be-Fe)	Be	–	227	–	4.18	11	
NGC 346-096	B1-2 (Be-Fe)	Be	–	343	–	4.18	11	
NGC 346-097	O9 V	37500	4.49	22	M06	4.75	22	
NGC 346-098	B1.5 V	26100	4.05	56	A	4.16	11	
NGC 346-099	B3 III	18000	3.40	94	He	3.79	7	
NGC 346-100	B1.5 V	26100	4.30	183	A	4.16	11	
NGC 346-101	B1 V	27300	4.25	29	A	4.18	12	
NGC 346-102	B3 III	17700	3.70	30	He	3.75	7	
NGC 346-103	B0.5 V	29500	4.00	10	H06	4.26	13	
NGC 346-104	B0 V	33500	4.45	17	He	4.41	16	Binary
NGC 346-106	B1 V	27500	4.20	142	He	4.17	12	Binary
NGC 346-107	O9.5 V	35900	4.23	55	M06	4.40	18	
NGC 346-108	B1.5 V	26100	3.95	167	A	4.11	11	
NGC 346-109	B1.5 V	26100	4.25	123	A	4.11	11	
NGC 346-110	B1-2 (Be-Fe)	Be	–	243	–	4.11	11	Binary
NGC 346-112	O9.5 V	34400	4.15	143	M06	4.36	17	
NGC 346-114	B1 Vn	27300	3.90	287	A	4.13	12	
NGC 346-116	B1 V	28250	4.10	15	H06	4.15	12	

Table 4. Atmospheric parameters and $v \sin i$ values of the NGC 330 sample. Symbols and labels are the same as given in Table 3.

Star	Spectral Type	T_{eff} (K)	$\log g$ (dex)	$v \sin i$ (km s^{-1})	Method	L/L_{\odot}	Mass (M_{\odot})	Comments
NGC 330-002	B3 Ib	14590	2.15	<24	T06	4.77	15	
NGC 330-003	B2 Ib	17210	2.25	<36	T06	4.89	16	Binary
NGC 330-004	B2.5 Ib	17000	2.30	<41	T06	4.81	15	
NGC 330-005	B5 Ib	13700	2.25	20	T06	4.58	13	
NGC 330-009	B5 Ib	13940	2.45	28	T06	4.45	12	
NGC 330-010	B5 Ib	14820	2.60	<15	T06	4.44	12	
NGC 330-013	O8.5 III-II((f))	34500	3.40	78	M06	5.40	32	
NGC 330-014	B1.5 Ib	20130	2.75	45	T06	4.69	14	
NGC 330-016	B5: II	14220	2.60	40	T06	4.24	10	
NGC 330-017	B2 II	22000	3.35	21	T06	4.66	14	
NGC 330-018	B3 II	18000	2.95	48	T06	4.45	12	
NGC 330-020	B3 II	16720	2.85	<42	T06	4.35	11	
NGC 330-021	B0.2 III	30500	3.70	204	He	4.95	21	
NGC 330-022	B3 II	18860	3.00	24	T06	4.42	12	
NGC 330-024	B5 Ib	14000	2.70	46	He	4.05	9	
NGC 330-025	B1.5e	Be	–	178	–	4.64	15	
NGC 330-026	B2.5 II	22500	3.40	73	T06	4.50	12	
NGC 330-027	B1 V	22040	3.20	80	T06	4.46	12	
NGC 330-028	B1 V	27300	3.75	76	A	4.63	15	
NGC 330-029	B0.2 V(Be-Fe)	Be	–	209	–	4.75	18	Binary
NGC 330-031	B0.5 V(Be-Fe)	Be	–	178	–	4.69	17	
NGC 330-032	B0.5 V	29700	4.15	17	T06	4.67	17	
NGC 330-033	B1.5 V	26100	3.90	105	A	4.53	14	
NGC 330-034	B1-2e	Be	–	231	–	4.53	14	
NGC 330-035	B3 II	19000	3.20	40	He	4.22	10	
NGC 330-036	B2 II	21200	3.25	39	A	4.33	11	
NGC 330-038	B1 V	27300	3.75	150	A	4.53	14	
NGC 330-039	B0 V	33000	4.25	120	He	4.72	18	
NGC 330-040	B2 III	21200	3.25	106	A	4.25	11	
NGC 330-041	B0 V	32000	4.15:	127	He	4.64	17	
NGC 330-042	B2 II	25450	3.75	27	T06	4.38	12	
NGC 330-043	B0 V	33000	4.10:	250	He	4.64	18	
NGC 330-044	B1-2 (Be-Fe)	Be	–	184	–	4.37	12	
NGC 330-045	B3 III	18450	3.25	133	A	4.01	9	Binary
NGC 330-046	O9.5 V	34000	4.25:	165	He	4.64	18	
NGC 330-047	B1 V	26700	4.00	28	T06	4.35	12	
NGC 330-048	B0.5 V	29000	4.00	73	He	4.42	14	
NGC 330-049	O9 V	35000	4.15	40	He	4.64	19	
NGC 330-050	B3e	Be	–	214	–	4.05	9	
NGC 330-051	B1.5 V	26100	4.05	273	A	4.30	12	
NGC 330-052	O8.5 Vn	35700	3.91	291	M06	4.60	19	
NGC 330-053	B0.5 V	29650	4.25	82	A	4.42	14	Binary
NGC 330-054	B2 (Be-Fe)	Be	–	147	–	4.25	8	
NGC 330-055	B0.5 V	31000	4.10	219	He	4.46	15	Binary?
NGC 330-056	B2 III	21200	3.50	108	A	4.06	9	
NGC 330-057	B0.5 V	29000	4.15	104	He	4.34	13	
NGC 330-058	B3:	SP?	–	263	–	3.97	10	
NGC 330-059	B3 III	18450	3.25	123	A	3.89	8	
NGC 330-060	B2.5 (Be-Fe)	Be	–	88	–	4.08	9	
NGC 330-062	B3e	Be	–	241	–	3.95	8	
NGC 330-063	B1-3	SP?	–	199	–	4.17	11	
NGC 330-064	B3:e	Be	–	269	–	3.93	8	
NGC 330-065	B1-3 (Be-Fe)	Be	–	284	–	4.13	11	
NGC 330-066	B3 III	18500	3.40	126	He	3.83	8	
NGC 330-067	B2.5 III	19850	3.40	65	A	3.90	8	

Table 4. -continued.

Star	Spectral Type	T_{eff} (K)	$\log g$ (dex)	$v \sin i$ (km s^{-1})	Method	L/L_{\odot}	Mass (M_{\odot})	Comments
NGC 330-068	B1.5 (Be-Fe)	Be	–	23	–	4.16	11	
NGC 330-069	B3 III	19000	3.40	193	He	3.85	8	
NGC 330-070	B0.5e	Be	–	348	–	4.29	13	
NGC 330-071	B3 III	19000	3.50	92	He	3.84	8	
NGC 330-072	B0.5 V	29650	4.15	99	A	4.29	13	
NGC 330-073	B8 Ib	12000	2.20	49	He	3.37	5	
NGC 330-074	B0 V	32020	4.20	29	T06	4.35	15	
NGC 330-075	B8 II	13500	3.20	166:	He	3.46	6	
NGC 330-076	B3 (Be-Fe)	Be	–	62	–	3.86	8	
NGC 330-079	B3 III	19500	3.40	146	He	3.82	8	Binary
NGC 330-080	B1-3	SP?	–	283	–	4.06	10	
NGC 330-081	B1-3	19000	3.50	190	He	3.79	7	
NGC 330-082	B1-3	SP?	–	192	–	4.05	10	
NGC 330-083	B3 III	18000	3.25	140	He	3.72	7	
NGC 330-084	B3 V-III	SB2?	–	26	–	3.83	8	Binary
NGC 330-085	B3:e	Be	–	191	–	3.82	8	
NGC 330-086	B2.5 III	19850	3.50	89	A	3.80	8	
NGC 330-087	Be-Fe	Be	–	214	–	3.81	8	
NGC 330-089	B1-5	18500	3.50	193	He	3.70	7	
NGC 330-090	B3 III	18450	3.30	167	A	3.69	7	
NGC 330-091	B0e	Be	–	272:	–	4.25	14	
NGC 330-094	B1-5	SP?	–	330	–	3.77	8	
NGC 330-095	B3 III	18450	3.45	20	A	3.67	7	
NGC 330-096	B1-3 (Be-Fe)	Be	–	175:	–	3.97	10	
NGC 330-097	B1 V	27300	3.90	154	A	4.05	11	
NGC 330-098	B0.2: V	SP?	–	148	–	4.18	13	
NGC 330-099	B2-3	SP?	–	187	–	3.86	9	
NGC 330-100	Be (B0-3)	Be	–	373	–	3.99	10	
NGC 330-101	B2.5 III	19850	3.50	48	A	3.73	7	
NGC 330-102	B2-3 III	19850	3.60	129	A	3.72	7	
NGC 330-103	B1-3	SP?	–	131	–	3.94	9	
NGC 330-104	B0: V	SP?	–	309:	–	4.19	14	
NGC 330-105	B1-3	SP?	–	13	–	3.91	9	
NGC 330-106	B1-2	SP?	–	71	–	3.95	10	
NGC 330-107	B3: V-III	16500	3.25	34	He	3.49	6	Binary
NGC 330-108	B5 III	14500	3.30	102	He	3.35	5	
NGC 330-109	B3 III	18450	3.20	213	A	3.60	7	
NGC 330-110	B2 III	21200	3.40	110	A	3.74	8	
NGC 330-111	B1-3	SP?	–	173	–	3.79	8	
NGC 330-112	B1-3 (Be-Fe)	Be	–	262	–	3.79	8	
NGC 330-113	B1-3	SP?	–	327	–	3.78	8	
NGC 330-114	B2 III	23800	3.90	17	T06	3.83	9	
NGC 330-116	B3 III	19500	3.55	4	He	3.62	7	
NGC 330-118	B1-2	SP?	–	32	–	3.89	10	
NGC 330-119	B1-3	SP?	–	265	–	3.84	9	
NGC 330-120	B3: V-III	18500	3.40	137:	He	3.47	6	
NGC 330-123	O9.5 V	35000	4.25:	26	He	4.58	18	
NGC 330-124	B0.2 V	30980	4.25	95	T06	4.42	15	
NGC 330-125	B2 III	21200	3.50	86	A	4.01	9	

Table 5. Atmospheric parameters and $v \sin i$ values of the N11 sample. Symbols and labels are the same as given in Table 3.

Star	Spectral Type	T_{eff} (K)	$\log g$ (dex)	$v \sin i$ (km s^{-1})	Method	L/L_{\odot}	Mass (M_{\odot})	Comments
N 11-001	B2 Ia	18750	2.50	<52	H06	5.66	38	
N 11-002	B3 Ia	15800	2.10	<53	H06	5.26	24	
N 11-003	B1 Ia	23200	2.75	<54	H06	5.42	30	
N 11-004	O9.7 Ib	31600	3.36	40	M06	5.80	48	
N 11-008	B0.5 Ia	25450	3.00	<43	H06	5.39	30	
N 11-009	B3 Iab	15000	2.15	30	H06	4.85	17	Binary
N 11-010	O9.5 III +B1-2	SB2	–	152	–	5.59	40	Binary
N 11-010B		SB2	–	12	–	–	–	Binary
N 11-011	OC9.5 II	29500	3.15	<60	He	5.49	35	Binary
N 11-012	B1 Ia	20500	2.55	40	H06	5.13	22	
N 11-014	B2 Iab	19100	2.55	30	H06	5.03	19	Binary
N 11-015	B0.7 Ib	23600	2.95	58	H06	5.23	24	
N 11-016	B1 Ib	21700	2.75	54	H06	5.13	22	
N 11-017	B2.5 Iab	16500	2.30	<25	H06	4.82	17	Binary
N 11-023	B0.7 Ib	24000	2.90	66	H06	5.09	21	
N 11-024	B1 Ib	21600	2.80	<30	H06	4.96	18	
N 11-026	O2.5 III(f*)	53300	4.00	109	M06	5.92	82	
N 11-029	OC9.7 Ib	28750	3.30	40	H06	5.21	25	
N 11-031	ON2 III(f*)	45000	3.85	116	M06	5.84	61	
N 11-032	O7 II(f)	35200	3.45	<65	M06	5.43	34	
N 11-033	B0 IIIIn	27200	3.21	256	M06	5.07	21	
N 11-034	B0.5 III	25500	3.25	203	He	5.03	20	Binary
N 11-035	O9 II(f)	31000	3.25	<56	He	5.23	27	Binary
N 11-036	B0.5 Ib	23750	3.10	30	H06	4.95	18	
N 11-037	B0 III	28100	3.25	100	H06	5.08	23	Binary
N 11-038	O5 III(f+)	41000	3.72	145	M06	5.69	48	
N 11-039	B2 III	21700	3.00	157	A	4.81	16	Binary?
N 11-040	B0: IIIIn	29500	3.30	273	He	5.11	24	
N 11-042	B0 III	29000	3.60	30	H06	5.05	22	Binary
N 11-045	O9-9.5 III	32300	3.32	105	M06	5.15	25	
N 11-046	O9.5 V	33500	4.25	205	He	5.21	28	Binary
N 11-047	B0 III	29200	3.65	55	H06	5.03	22	Binary
N 11-048	O6.5 V((f))	40700	4.19	130	M06	5.38	37	
N 11-051	O5 Vn((f))	42400	3.75	333	M06	5.31	36	
N 11-052	O9.5 V	SB2	–	16	–	5.23	29	Binary
N 11-054	B1 Ib	23500	3.05	45	H06	4.79	16	
N 11-056	B1e	Be/SB2	–	205	–	4.89	19	Binary
N 11-056B		Be/SB2	–	25	–	–	–	Binary
N 11-058	O5.5 V((f))	41300	3.89	85	M06	5.27	34	
N 11-059	O9 V	34000	3.85	103	He	5.13	26	Binary
N 11-060	O3 V ((f*))	45700	3.92	106	M06	5.57	49	
N 11-061	O9 V	33600	3.51	87	M06	5.20	27	
N 11-062	B0.2 V	30400	4.05	25	H06	4.95	21	Binary
N 11-063	O9: V	35000	4.25	196	He	5.11	26	
N 11-064	B0.2: Vn	SB2?	–	206	–	4.92	20	Binary?
N 11-065	O6.5 V((f))	41700	3.89	83	M06	5.17	33	
N 11-066	O7 V((f))	39300	3.87	71	M06	5.10	30	
N 11-068	O7 V((f))	39900	4.13	54	M06	5.06	29	
N 11-069	B1 III	24300	3.30	80	H06	4.63	15	
N 11-070	B3 III	19500	3.30	62	He	4.40	12	
N 11-072	B0.2 V	28800	3.75	15	H06	4.77	18	
N 11-073	B0.5 (Be-Fe)	Be	–	222	–	4.78	18	
N 11-074	B0.5 (Be-Fe)	Be	–	169	–	4.78	18	
N 11-075	B2 III	21800	3.35	25	H06	4.48	12	Binary
N 11-076	B0.2 Ia	26500	2.90	72	He	4.67	16	

Table 5. -continued.

Star	Spectral Type	T_{eff} (K)	$\log g$ (dex)	$v \sin i$ (km s^{-1})	Method	L/L_{\odot}	Mass (M_{\odot})	Comments
N 11-077	B2 III	21500	3.30	117	He	4.47	12	Binary
N 11-078	B2 (Be-Fe)	Be	–	93	–	4.59	14	Binary
N 11-079	B0.2 V	32500	4.25	38	He	4.88	21	
N 11-081	B0:n (Be-Fe)	Be	–	363	He	4.79	19	
N 11-082	B1-2 +early B	SB2	–	95	–	4.58	14	Binary
N 11-082B		SB2	–	110	–	–	–	Binary
N 11-083	B0.5 V	29300	4.15	20	H06	4.71	17	Binary
N 11-084	B0.5 V	29500	4.25	108	He	4.75	18	Binary
N 11-085	B0.5 V	SB2	–	105	–	4.73	17	Binary
N 11-085B		SB2	–	28	–	–	–	Binary
N 11-086	B1 V	26800	4.25	75	A	4.65	16	
N 11-087	O9.5 Vn	32700	4.04	276	M06	4.91	21	
N 11-088	B1 III	24150	3.45	240	A	4.54	14	
N 11-089	B2 III	21700	3.20	117	A	4.42	12	Binary
N 11-090	B2e	Be	–	104	–	4.53	14	
N 11-093	B2.5 III	19500	3.30	73	He	4.29	11	
N 11-094	B1 III	SB2	–	147	–	4.50	13	Binary
N 11-095	B1 Vn	26800	3.85	267	A	4.59	15	
N 11-096	B1 III	SB2	–	32	–	4.49	13	Binary
N 11-097	B3 II	17500	2.95	52	He	4.17	10	
N 11-098	B2 III	21700	3.50	45	A	4.37	12	Binary
N 11-100	B0.5 V	29700	4.15	30	H06	4.68	17	
N 11-101	B0.2 V	29800	3.95	70	H06	4.68	17	
N 11-102	B0.2 V	31000	4.20	218	He	4.73	18	
N 11-103	B1-2 + early B	SB2	–	125	–	4.53	14	Binary
N 11-103B		SB2	–	80	–	–	–	Binary
N 11-104	B1.5 V	25700	3.75	153	A	4.52	14	
N 11-105	B1 V	SB2?	–	116	–	4.56	15	Binary?
N 11-106	B0 V	31200	4.00	25	H06	4.72	18	
N 11-107	B1-2 + early B	SB2	–	80	–	4.51	13	Binary
N 11-107B		SB2	–	170	–	–	–	Binary
N 11-108	O9.5 V	32150	4.10	25	H06	4.73	19	
N 11-109	B0.5 Ib	25750	3.20	40	H06	4.48	12	
N 11-110	B1 III	23100	3.25	25	H06	4.37	12	
N 11-111	B1.5 III	22950	3.50	101	A	4.36	12	
N 11-113	B0.5 III	SB2	–	38	–	4.49	14	Binary
N 11-113B		SB2	–	20	–	–	–	Binary
N 11-114	B0 Vn	32500	4.05	299	He	4.70	19	
N 11-115	B1 III	24150	3.65	53	A	4.39	12	
N 11-116	B2 III	21700	3.30	160	A	4.28	11	
N 11-117	B1 Vn	26800	4.20	247	A	4.46	13	
N 11-118	B1.5 V	25700	3.80	150	A	4.42	13	Binary
N 11-119	B1.5 V	SB2	–	259	–	4.42	13	Binary
N 11-120	B0.2 Vn	31500	4.10	207	He	4.63	17	
N 11-121	B1 Vn	26800	4.20	265	A	4.45	14	
N 11-122	O9.5 V	33000	4.10	173	He	4.62	18	
N 11-123	O9.5 V	34800	4.22	110	M06	4.58	19	
N 11-124	B0.5 V	28500	4.20	45	H06	4.47	14	Binary

Table 6. Atmospheric parameters and $v \sin i$ values of the NGC 2004 sample. Symbols and labels are the same as given in Table 3.

Star	Spectral Type	T_{eff} (K)	$\log g$ (dex)	$v \sin i$ (km s^{-1})	Method	L/L_{\odot}	Mass (M_{\odot})	Comments
NGC 2004-003	B5 Ia	14450	2.10	33	T06	5.04	20	Binary
NGC 2004-005	B8 Ia	12390	1.90	30	T06	4.95	18	Binary
NGC 2004-007	B8 IIa	12250	2.00	<30	T06	4.90	17	
NGC 2004-010	B2.5 Iab	17160	2.40	<30	T06	5.02	19	
NGC 2004-011	B1.5 Ia	21250	2.75	<40	T06	5.22	24	
NGC 2004-012	B1.5 Iab	21270	2.87	<40	T06	4.92	18	
NGC 2004-013	B2 II	21700	3.20	145	A	4.94	18	
NGC 2004-014	B3 Ib	17800	2.85	<30	T06	4.72	15	
NGC 2004-015	B1.5 II	22950	3.15	165	A	4.96	18	Binary
NGC 2004-020	B1.5 II	22950	3.20	145	A	4.91	18	Binary
NGC 2004-021	B1.5 Ib	21450	3.00	<40	T06	4.82	16	
NGC 2004-022	B1.5 Ib	21780	3.15	<30	T06	4.79	16	
NGC 2004-023	B2 (Be-Fe)	Be	–	102:	–	4.85	17	Binary?
NGC 2004-024	B1.5 IIIIn	22950	3.05	240	A	4.72	15	
NGC 2004-025	B2 (Be-Fe)	Be	–	83	–	4.75	15	Binary
NGC 2004-026	B2 II	22900	3.65	<20	T06	4.68	15	Binary
NGC 2004-027	B0e	Be	–	182:	–	5.00	23	
NGC 2004-029	B1.5e	23100	3.50	30	T06	4.65	14	Binary
NGC 2004-030	B0.2 Ib	29000	3.75	123	He	4.87	19	Binary
NGC 2004-031	B2 II	21700	3.35	65	A	4.58	13	Binary
NGC 2004-032	B2 II	21700	3.40	110	A	4.58	13	
NGC 2004-035	B1: (Be-Fe)	Be	–	244:	–	4.74	17	
NGC 2004-036	B1.5 III	22870	3.35	42	T06	4.58	13	
NGC 2004-039	B1.5e	Be	–	212:	–	4.67	15	
NGC 2004-041	B2.5 III	20450	3.30	101	A	4.43	12	Binary
NGC 2004-042	B2.5 III	20980	3.45	42	T06	4.45	12	
NGC 2004-043	B1.5 III	22950	3.50	24	A	4.52	13	
NGC 2004-044	B1.5:	SB2	–	18	–	4.62	15	Binary
NGC 2004-044B		SB2	–	55	–	–	–	Binary
NGC 2004-045	B2 III	21700	3.50	128	A	4.46	12	Binary
NGC 2004-046	B1.5 III	26090	3.85	32	T06	4.62	15	
NGC 2004-047	B2 III	21700	3.35:	133	A	4.42	12	Binary
NGC 2004-048	B2.5e	Be	–	173	–	4.49	13	
NGC 2004-050	B2.5 III	20450	3.30	109	A	4.35	11	Binary
NGC 2004-051	B2 III	21700	3.40	70	A	4.40	12	
NGC 2004-052	B2 III	21700	3.60	138	A	4.40	12	
NGC 2004-053	B0.2 Ve	31500	4.15	7	T06	4.77	18	
NGC 2004-054	B2 III	21700	3.40	114	A	4.39	12	Binary
NGC 2004-055	B2.5 III	20450	3.30	118	A	4.33	11	
NGC 2004-056	B1.5e	Be	–	229	–	4.52	14	
NGC 2004-058	O9.5 V (Nstr)	33500	4.10	195	He	4.80	20	Binary
NGC 2004-059	B2 III	21700	3.45	91	A	4.35	11	Binary
NGC 2004-060	B2 III	21700	3.45	134	A	4.35	11	
NGC 2004-061	B2 III	20990	3.35	40	T06	4.31	11	
NGC 2004-062	B0.2 V	30250	4.35	106	A	4.67	17	
NGC 2004-063	B2 III	21700	3.50	107	A	4.32	11	
NGC 2004-064	B0.7-B1 III	25900	3.70	28	T06	4.48	13	
NGC 2004-065	B2.5 III	20450	3.40	223	A	4.25	11	Binary?
NGC 2004-066	B1.5 Vn	25700	3.70	238	A	4.48	13	
NGC 2004-067	B1.5e	Be	–	237	–	4.48	13	
NGC 2004-068	B2.5 III	20450	3.65	62	A	4.25	11	
NGC 2004-069	B0.7 V	28000	4.00	178	He	4.54	15	
NGC 2004-070	B0.7-B1 III	27400	3.90	46	T06	4.51	14	
NGC 2004-071	B1.5 III	22950	3.50	98	A	4.33	12	
NGC 2004-073	B2 III	21700	3.55	37	A	4.26	11	

Table 6. -continued.

Star	Spectral Type	T_{eff} (K)	$\log g$ (dex)	$v \sin i$ (km s^{-1})	Method	L/L_{\odot}	Mass (M_{\odot})	Comments
NGC 2004-074	B0.7-B1 V	27375	4.25	130	A	4.49	14	Binary
NGC 2004-075	B2 III	21700	3.55	116	A	4.26	11	
NGC 2004-076	B2.5 III	20450	3.65	37	A	4.20	10	
NGC 2004-077	B0.5 V	29500	4.00:	215	He	4.56	16	
NGC 2004-078	B2 III	21700	3.55	115	A	4.26	11	Binary
NGC 2004-079	B2 III	21700	3.60	165	A	4.25	11	Binary
NGC 2004-080	B2.5 III	20450	3.40	85	A	4.19	10	
NGC 2004-081	B1 V	26800	4.00	105:	A	4.45	13	
NGC 2004-082	B1.5 V	25700	4.10	161	A	4.42	13	
NGC 2004-083	B1.5:e Be	—	—	194	—	4.42	13	Binary
NGC 2004-084	B1.5 III	27395	4.00	36	T06	4.46	14	
NGC 2004-085	B2.5 III	20450	3.40	150	A	4.18	10	
NGC 2004-086	B2 III	21700	3.85	14	A	4.24	11	
NGC 2004-087	B1.5 V	25700	4.40	35	A	4.40	13	
NGC 2004-088	B2.5 III	20450	3.65	200:	A	4.18	10	Binary
NGC 2004-089	B2.5e Be	—	—	288	—	4.31	12	
NGC 2004-090	O9.5 III	32500	4.10	16	T06	4.64	17	
NGC 2004-091	B1.5 III	26520	4.05	40	T06	4.42	13	Binary
NGC 2004-092	B2e Be	—	—	171	—	4.34	12	
NGC 2004-093	B3 III	20000	3.65:	189:	He	4.14	10	Binary
NGC 2004-094	B2.5 III	20450	3.40	84:	A	4.16	10	Binary
NGC 2004-095	B1.5 V	25700	4.10	138	A	4.38	13	
NGC 2004-096	B1.5e Be	—	—	245	—	4.38	13	
NGC 2004-097	B2 III	21700	3.60	62	A	4.20	10	
NGC 2004-098	B2 III	21700	3.75	90	A	4.20	10	
NGC 2004-099	B2 III	21700	3.40	119	A	4.19	10	
NGC 2004-100	B1 Vn	26800	3.70	323	A	4.38	13	
NGC 2004-101	B2 III	21700	3.45	131	A	4.18	10	
NGC 2004-102	B2 III	SB2?	—	64:	—	4.18	10	Binary
NGC 2004-103	B2 III	21700	3.85	35	A	4.18	10	
NGC 2004-104	B1.5 V	25700	3.90	274	A	4.34	12	
NGC 2004-105	B1.5 V	25700	3.90	235	A	4.34	12	
NGC 2004-106	B2 III	21700	3.50	41	A	4.17	10	
NGC 2004-107	B0.5 V	28500	3.90	146	He	4.43	14	Binary
NGC 2004-108	B2.5 III	22600	4.00	13	T06	4.21	10	Binary
NGC 2004-109	B2.5 III	20450	3.50	41	A	4.11	10	Binary
NGC 2004-110	B2 III	21700	3.40	121	A	4.17	10	
NGC 2004-111	B2.5 III	20450	3.30	55	A	4.08	9	
NGC 2004-112	B2 III	21700	3.65	72	A	4.14	10	
NGC 2004-113	B2.5 III _n	20450	3.25	307:	A	4.08	9	
NGC 2004-114	B2 III	21700	3.60	59	A	4.12	10	
NGC 2004-115	B2e Be	—	—	8	—	4.24	11	Binary
NGC 2004-116	B2 III	21700	3.55	63	A	4.12	10	
NGC 2004-117	B2 III	21700	3.60	75	A	4.11	10	
NGC 2004-118	B1.5 V	SB2?	—	90:	—	4.25	12	Binary
NGC 2004-119	B2 III	23210	3.75	15	T06	4.15	10	